Phonon scattering and magnetic manifold switching in (GdSm)CrO_3

S. Das [1], R. K. Dokala [1], B. Weise [2], P. K. Mishra [1], R. Medwal [3], R. S. Rawat [4], and S. Thota [1,*]

[1] *Department of Physics, Indian Institute of Technology Guwahati, Guwahati 781039, Assam, India*

[2] *Leibniz-IFW Dresden, Institute for Complex Materials, D-01069 Dresden, Germany*

[3] *Department of Physics, Indian Institute of Technology Kanpur, Kanpur 208 016, Uttar Pradesh, India*

[4] *Natural Sciences and Science Education, National Institute of Education, Nanyang Technological University, Singapore 637616, Singapore*

(Received 8 April 2023; accepted 26 July 2023; published 22 August 2023)

We report on the temperature dependence of selective phonon scattering and magnetization switching in (GdSm)CrO_3 perovskites. Thermal evolution of key phonon modes $A_{1g}(6/5/3)$ and their anomalous change across the antiferromagnetic (AFM) Néel temperature ($T_N \sim 202$ K) endorses the strong spin-phonon coupling in the investigated system. Such changes have been identified in consonance with the vibrational spectrum of trivalent Gd and Cr along with antistretching/bending of Gd/Sm-O_{12} polyhedra and CrO_6 octahedra. Further, we find the emergence of many interesting features, such as thermomagnetic irreversibilities of the magnetization, significant enhancement of the ordering temperatures (up to 202 K), and multiple magnetization switching below T_N (9.7–85 K) upon the substitution of Sm at Gd sites. We find the presence of kinetic arrest of magnetic phases [$\Gamma_4(G_x, A_y, F_Z; F_R)$ and Γ_2 (F_x, C_y, G_z; F_x^R, C_y^R)] along with the presence of nonequilibrium frozen AFM and ferromagnetic clusters (<30 K with 70.7% frozen fraction), indicating the presence of a magnetic glassy state which assists the Γ_4-to-Γ_2 phase transition and supports the phase-coexistence nature of the (GdSm)CrO_3 perovskites. Interestingly, Sm moments order across 6.82 K (T_N^{Sm}), giving rise to yet another phase transition: Γ_{26} (C_x , G_y , C_x ; C_x^R, A_y^R, F_z^R)/Γ_{27} (F_x , C_y , G_z ; F_x^R, C_y^R, G_z^R). On the other hand, field-dependent (100 Oe $\leqslant H_{DC} \leqslant$ 600 Oe) bipolar switching of magnetization ($-7.8/+2.1/-12/+16$ emu/mol) at different temperatures below T_N under different measurement protocols makes the investigated system a suitable candidate for the magnetic memories and magnetic switches.

DOI: 10.1103/PhysRevMaterials.7.084410

I. INTRODUCTION

Over the course of the last few decades, the rare-earth orthochromites ($RCrO_3$, where R is the symbol for a rare-earth element) have been subjected to extensive research utilizing a wide variety of different characterization techniques such as neutron diffraction, heat capacity, Mossbauer analysis, and magnetodielectric and optical-absorption spectroscopy [1–3]. These techniques have been widely used to probe the ferroelectricity driven by the coexistence of local noncentral symmetry and multiple magnetic ordering [antiferromagnetic (AFM) and ferromagnetic (FM) behavior] in $RCrO_3$. In addition to these features, phenomena such as exchange bias, spin-reorientation transitions, negative magnetization and its reversal, and spin-glass states have been the subject of substantial research in $RCrO_3$-related systems [1–5]. The phenomenon of magnetization reversal observed in these compounds is highly intriguing and has garnered significant scientific interest due to the distinct temperature dependence of magnetic moments between the cations of the constituent sublattices. In systems related to $RCrO_3$, a noteworthy feature is the occurrence of the magnetic compensation effect. This effect is observed when the two sublattices within the system balance each other, resulting in a compensation point (T_{Comp}) at a specific temperature. At this temperature, the net magnetization undergoes a transition from positive to negative polarity, depending on the specific measurement protocol employed [6]. The phenomenon of magnetization reversal is widely recognized as being dependent on the existence of two distinct states of magnetization. This characteristic renders the materials highly suitable for the development of switchable devices, including but not limited to volatile magnetic memory storage, thermomagnetic switches, high-speed read/write magnetic memories, and thermally assisted magnetic random-access memory [7,8]. Typically, most materials demonstrate a magnetic-compensation effect at T_{Comp} that is significantly lower than room temperature, thereby restricting their potential utility in magnetoelectronic devices. Hence, it is crucial from a research perspective to acquire a more comprehensive understanding of the tunability of T_{Comp} at elevated temperatures for these applications. The internal field induced by the transition metal oxide sublattice (Cr^{3+}, Mn^{3+}, etc.) plays a major role in magnetization reversal of $RCrO_3$-related systems, in which rare-earth elements (Gd^{3+} and/or Ce^{3+}) couple antiferromagnetically with transition metal ions which polarize them to get aligned in the opposite direction (with respect to the applied field), causing reversal in the magnetization [9]. Most $RCrO_3$ materials (e.g., $PrCrO_3$, $YbCrO_3$, $HoCrO_3$) display the magnetization reversal under the field-cooled warming (FCW) protocol. However, the first end compound $GdCrO_3$ exhibits negative magnetization only

*subhasht@iitg.ac.in

under the field-cooled cooling (FCC) mode, indicating the interesting measurement protocol/history-dependent features [10].

On the other hand, the second end compound $SmCrO_3$ is another intriguing system which shows negative magnetization under the zero-field-cooled warming (ZFCW) protocol [11]. Interestingly, this newly emerging compound displays multiferroicity and a temperature-dependent rapid spin-reorientation phase transition. The abrupt spin-reorientation characteristic, which occurs over short distances, holds significant potential for utilization in various applications such as thermomagnetic power generation, magnetic refrigeration, and spin-switching devices [12,13]. The emergence of metastable glass is attributed to the disparity in free energies, wherein the metastable state endures with fluctuating energy levels below the threshold at which the low-temperature ordered phase commences by surpassing the energy barrier [14,15]. The phenomenon of thermomagnetic history-dependent kinetic arrest is indicative of the slowing down of the growth of the AFM phase in comparison with the FM phase, due to its viscous retardation. Recent studies have found this exceptional feature in various strongly correlated systems like $Ce(Fe_{0.96}Ru_{0.04})_2$ [16], $La_{0.5}Ca_{0.5}MnO_3$ [14], $Fe_{0.955}Ni_{0.045}Rh$ [15], Gd_5Ge_4 [17], and $SmCrO_3$ [18]. Authors of some recent studies also suggest low-temperature spin-glasslike features in $SmCrO_3$ and related compounds [18]. Here, both end compounds $GdCrO_3$ and $SmCrO_3$ crystallize in orthorhombic structure (*Pbnm* space group) with AFM ordering temperature at 171 and 192 K with Γ_4 (G_x, A_y, F_Z; F_R) spin configuration and go through spin reorientation at 7 and 37 K, respectively, with Γ_2 (F_x, C_y, G_z; F_x^R, C_y^R) spin alignment. While $GdCrO_3$ attains a high isothermal entropy change of $36.9\,J\,kg^{-1}\,K^{-1}$ with adiabatic temperature change ΔT of $\sim$19 K [with relative cooling capacity of $542\,J\,kg^{-1}$ (for $\Delta H \sim 7$ T)], which is quite useful for the magnetic refrigeration [19], on the other hand, $SmCrO_3$ shows the conventional field-cooled negative exchange bias field as high as 4709 Oe at 10 K. Moreover, below the spin-reorientation temperature ($\sim$33 K) spin-glasslike features have been noticed in this system where the high-temperature Γ_4 state coexists with the Γ_2 state [20].

Here, in this article, we report on a comprehensive study of the crystal structure, phonon spectroscopy, and the magnetic properties of both end compounds $GdCrO_3$ and $SmCrO_3$ with few intermediate compositions prepared by the standard solid-state reaction method. Here, Sm is substituted at Gd sites of the $GdCrO_3$ system. We considered the following three compositions: 10, 50, and 90% of Sm at the A-site of $GdCrO_3$ that exhibits complex Cr^{3+}-Cr^{3+} and R^{3+} (Gd^{3+}, Sm^{3+})-Cr^{3+} interactions, which is responsible for the multiple T_{Comp} over a wide temperature interval. There is a notable absence of extensive study on temperature-dependent Raman spectroscopy in the existing literature. Our findings effectively address this gap by providing a comprehensive investigation of temperature dependence, thereby contributing to a more thorough understanding of the subject matter. The high $T_{Comp} \sim 195$ K noticed under the ZFCW protocol and large negative magnetization ($\sim$17 emu/mol) within the narrow temperature region make the investigated system attractive for applications in magnetoelectronics. In the subsequent section, we present the experimental methodology and analyze the obtained results in relation to previously documented data on analogous systems, accompanied by a comparative examination of all the findings. We have successfully established correlations among the various findings and have subsequently presented our concluding remarks and future prospects.

II. EXPERIMENTAL DETAILS

The polycrystalline $Gd_{1-x}Sm_xCrO_3$ (GSO) perovskites with compositions $x = 0.1$ (GSO1), 0.5 (GSO5), and 0.9 (GSO9) were prepared using the standard solid-state reaction method at high sintering temperatures and atmospheric pressure, the primary materials being gadolinium (III) oxide (Gd_2O_3), samarium (III) oxide (Sm_2O_3), and chromium (III) oxide (Cr_2O_3) with 99.9% purity. These binary oxides were mixed according to the proper stoichiometric proportions for 5 h in air using an agate mortar and pestle to obtain a homogeneous mixture. This product was calcined in an alumina crucible at 1000 °C for 12 h in air followed by regrinding for 2 h and pelletizing by applying 60 kN pressure using a hydraulic press. These pellets were sintered at 1200 °C for 36 h in air and slowly cooled in air to room temperature. This process leads to grain growth and attains high density without any pores inside the pellet. The x-ray powder diffraction (XRD) measurements of the samples were carried out using an x-ray powder diffractometer of model Rigaku, TTRAX III, equipped with Cu-$K\alpha_1$ radiation ($\lambda = 1.54056$ Å) as the laser source. The diffraction angle (2θ) variation was kept between 10° and 90° with slow scan speed of 2°/min with step size $\sim$0.02. These studies confirm the monophasic nature of the samples. Moreover, the crystallographic parameters and other relevant data have been extracted by means of a Rietveld refinement method using the FULLPROF suite. An x-ray photoelectron spectroscope (XPS) was used to probe the electronic structure and oxidation state of the constituent elements (Gd, Sm, Cr, and O) to complement the phase purity. These measurements were performed using a high-resolution PHI 5000VVersaProbe III scanning XPS with microprobe Al-$K\alpha$ (544 eV). The core-level x-ray photoelectron spectra were calibrated with C-1*s* binding energy 282.6 eV. To characterize the vibrational excitations, a detailed Raman spectrum was recorded using a HR Raman spectrometer (model LabRam HR) from Horiba Jobin Yvon using monochromatic radiation of wavelength $\lambda \sim 632.8$ nm He-Ne laser (20 mW laser power) operating under backscattering geometry. A temperature-dependent Raman study has been performed down to the liquid-nitrogen temperature 80 K from 300 K using the THMS600 module. For a precise understanding of the magnetic structure of GSO, we performed the DC magnetization measurements using a physical property measurement system from Quantum Design (model Dynacool) assembled with a vibrating sample magnetometer accessory. The magnetization data have been recorded between the temperatures 1.9 and 300 K for different magnetic fields ($H \sim \pm 90$ kOe). Several measurement protocols have been utilized for the purpose of measuring magnetization, including the ZFCW, FCW, and FCC protocols. In the subsequent section, we present the outcomes and examination related to these experiments.

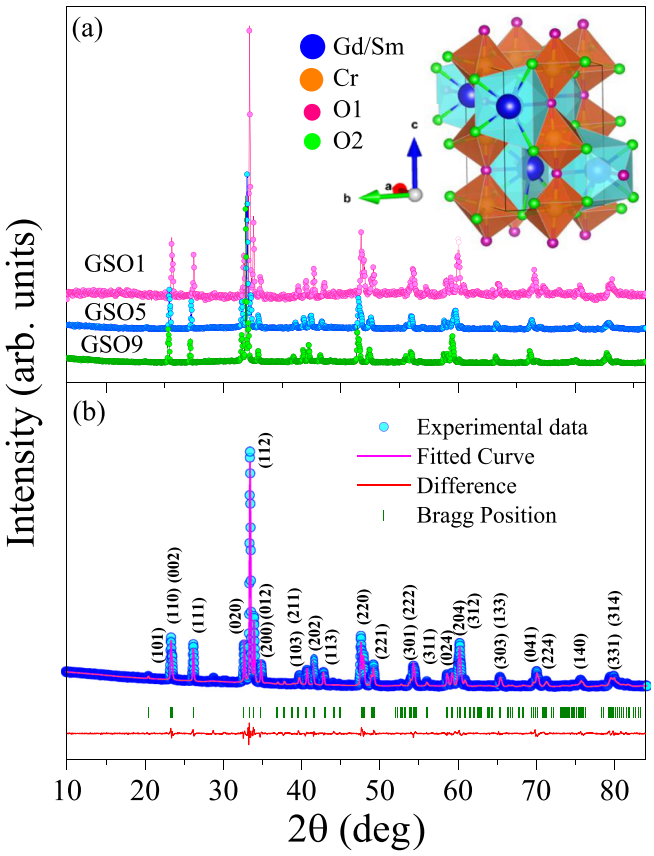

FIG. 1. (a) The x-ray diffraction (XRD) patterns recorded at room temperature of $Gd_{0.9}Sm_{0.1}CrO_3$ (GSO1), $Gd_{0.5}Sm_{0.5}CrO_3$ (GSO5), and $Gd_{0.1}Sm_{0.9}CrO_3$ (GSO9) samples represented as pink, blue, and green lines, respectively. (b) The XRD of GSO5 along with Rietveld refinement data considering *Pbnm* space group of distorted orthorhombic systems. The blue spheres represent the experimental data; pink, red, and green lines refer to the fitted curve, difference, and Bragg positions, respectively. The inset of (a) shows the unit-cell structure of $Gd_{0.5}Sm_{0.5}CrO_3$, where blue, white, yellow, pink, and green spheres symbolize Gd, Sm, Cr atoms, and apical (O1) and basal (O2) oxygen, respectively.

III. RESULTS AND DISCUSSION

A. Crystal structure analysis

We begin our analysis with the crystal structure for different compositions of the investigated systems. The associated crystallographic cell parameters are calculated and analyzed by means of powder XRD for all three compositions of GSO with $x = 0.1$, 0.5, and 0.9. Figure 1(a) shows the XRD patterns of GSO1, GSO5, and GSO9 along with the Rietveld refinement data of GSO5 [Fig. 1(b)], which confirm the perovskite structure and the phase purity with goodness of the fit $\chi^2 = 2.67$ for GSO5. The unit cell structure obtained from VESTA after refinement for the same sample is displayed in the inset of Fig. 1(a). Here, the blue spheres represent A-site cations (Gd^{3+}/Sm^{3+}), and yellow spheres show the B-site Cr^{3+} ions, while the apical and basal equilateral oxygen atoms have been represented with smaller pink and green spheres. The A-site cations move in opposite directions with respect to each other in CrO_6 octahedra in both in-phase and out-phase tilting with respect to [001] and [110] axes. All Bragg peaks are indexed using *Pbnm* space group (No. 62) with distorted orthorhombic perovskite structure, where the absence of any extra peak signals the system is devoid of any secondary phase. The refined lattice parameters are listed in Table 1s in the Supplemental Material [21]. The hole-doped GSO with Sm substitution at some of the Gd cations shows an increment in the cell parameter a and a reduction in b and c due to the larger cationic radius of Sm^{3+} (∼1.079 Å with VIII coordination number) than that of Gd^{3+} (∼1.053 Å with VIII coordination number) [9,22,23]. The occupancy of two A-site cations (Sm and Gd) at the same crystallographic site induces the disorder in the unit cell which has been characterized using the average radius of A-site cations as calculated by

$$R_{\mathrm{Avg}} = \sqrt{(1-x)R^2_{\mathrm{Gd}^{3+}} + xR^2_{\mathrm{Sm}^{3+}}}, \tag{1}$$

where $R_{\mathrm{Gd}^{3+}}$ and $R_{\mathrm{Sm}^{3+}}$ are the radii of the Gd and Sm cations, respectively. From Table 1s in the Supplemental Material [21], a distinct anomaly in volume and lattice parameter c occurs for $x = 0.5$ and changes thereafter for further increase of x. To understand and validate the above scenario, the other cell parameters are systematically evaluated. Here, the tolerance factor is calculated by Goldschmidt's formula, as given below:

$$t = \frac{(1-x)R_{\mathrm{Gd}^{3+}} + xR_{\mathrm{Sm}^{3+}} + R_{\mathrm{O}^{2-}}}{\sqrt{(R_{\mathrm{Cr}^{3+}} + R_{\mathrm{O}^{2-}})}}. \tag{2}$$

The value of t exhibits an upward trend as the amount of Sm substitution at the Gd sites increases, suggesting that the unit cell becomes more stable and approaches the *Pm*3*m* ideal cubic space group. Here, two types of oxygen atoms are denoted by apical oxygen (O1) and basal equilateral oxygen (O21 and O22). The sudden reduction in the octahedral distortion (Δ) by one factor for GSO5 can be attributed to the drop of the b axis length by 0.4% which increases rapidly with increasing the Sm substation from $x = 0.5$ to 0.9. Further, the averaged bond distances $d_{(\mathrm{Cr\text{-}O})}$ between IX-coordinated Cr and all the basal and apical oxygen atoms for $N = 6$ has been calculated by considering the magnitude of Δ as reported in Ref. [24]. The average Cr-O21 bond length changes exactly in the reverse way as that of Cr-O22 with Sm^{3+} substitution, which indicates the shrinking of one basal-oxygen-Cr bond with elongation of the another, keeping the whole trend constant overall inside CrO_6 octahedra. A similar anomaly in the bond length has been noticed for the GSO5 system as well. The in-phase (θ) and out-phase (φ) tiltings with respect to [110] and [001] axes have been calculated using $\theta = \frac{180^\circ - [\mathrm{Cr-O(1)-Cr}]}{2}$ and $\cos\varphi = \cos\frac{90^\circ - [\mathrm{Cr-O(2)-Cr}]/2}{\sqrt{\cos\theta}}$, which are listed in Table 1s in the Supplemental Material [21]. We noticed a prominent change in GSO5 pointing toward the minimum and maximum bendings of the CrO_6 octahedra, which is in line with the bond length variation as well. The large rare-earth cation size shares bond angles between both the apical and basal oxygen atoms that increases from 2.356 to 2.749 Å and 2.341 to 2.544 Å for the compositions GSO1-GSO9, respectively, confirming the high sensitivity of oxygen affinity of the rare earth. Inside the CrO_6 octahedra, the bond angles between Cr-O1-Cr and Cr-O2-Cr show a similar trend (Table 1s in the Supplemental Material [21]), in line with the

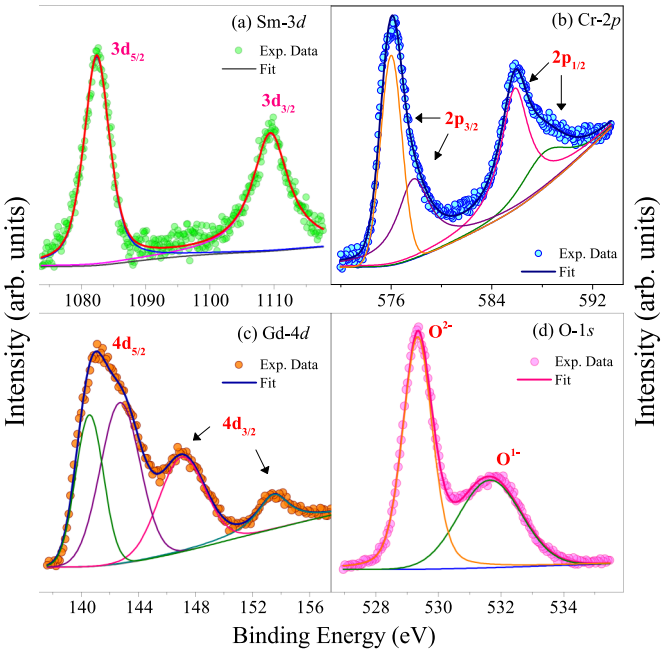

FIG. 2. The x-ray photoemission spectra of the individual elements of GSO5 bulk polycrystalline sample: (a) Sm-3*d* (green), (b) Cr-2*p* (blue), (c) Gd-4*d* (orange), and (d) O-1*s* (pink) core levels. Here, the spheres represent the experimentally obtained data points, while the solid lines represent the peak fitting data. The phase purity can be justified with the proper oxidation states of the constituent elements.

previously specified parameters. Simultaneously, the notable anomaly and persistent deviation of the tilting angles and octahedral distortion resulting from Sm/Gd substitution are likely to exert a significant impact on the magnetic properties and Raman spectra, as elaborated in the subsequent discussion.

B. Electronic structure and x-ray photoelectron spectroscopy

To investigate the electronic structure of the synthesized perovskites, XPS studies were conducted. This analytical technique allows for the determination of the oxidation states of the constituent elements, thereby verifying the phase purity of the system. Figure 2 shows the XPS spectra of the GSO5 system. Using these spectra, the surface-level electronic structures of the elements are studied. All core level spectra have been calibrated with the C-1*s* binding energy peak located at 285 eV. The Tougaard algorithm is utilized for the purpose of background correction, and the various chemically distinct states are determined through the application of least square fitting to the experimental data. The binding energy dependence of the ejected photoelectron intensity is probed for each of the elements separately: (a) Sm-3*d* (b) Cr-2*p*, (c) Gd-4*d*, and (d) O-1*s*. Here, the Sm-3*d* core level spectra [Fig. 2(a)] are deconvoluted into two peaks cantered at 1082.2 and 1109.4 eV.

The lower binding energy peak is attributed to the $3d_{5/2}$ state, while the higher energy peak is a result of the $3d_{3/2}$ state. The presence of two distinct peaks, with a significant binding energy difference of approximately $\Delta \sim 27$ eV, is commonly attributed to the spin-orbit coupling phenomenon. This observation serves as confirmation of the trivalent oxidation state of Sm [25]. The deconvolution of the Gd-4*d* core-level spectra [as shown in Fig. 2(c)] necessitates the utilization of four distinct spectral lines. These lines comprise two doublets that are linked to the $4d_{5/2}$ and $4d_{3/2}$ core levels. The peaks observed at energy levels of 140.7, 142.7, 146.8, and 153.2 eV have been identified and categorized based on the experimental data provided in the available literature. Here, Gd with xenon-like configuration with a filled *s* orbital and singly occupied *f* and *d* orbitals get oxidized to Gd^{3+}, indicating the presence of a trivalent state of Gd. The splitting of the 4*d* orbitals due to spin-orbit coupling in $4d_{5/2}$ (146 and 153 eV) and $4d_{3/2}$ core levels (140 and 142 eV) is detectable. No additional transitions related to the electronic state of the constituent elements under investigation were observed in this case, thus confirming the purity of the sample. On the other hand, the Cr-2*p* spectra [Fig. 2(b)] consist of four peaks at 575.8, 577.9, 585.5, and 588.3 eV, which are consistent with the range given in the standard XPS database of NIST [26]. The peaks at 585 eV and 588 eV are originating due to the doublet of the $2p_{1/2}$ electronic state, and the other two peaks are ascribed to the $2p_{3/2}$ state with no signatures of any satellite peak. In this case, the spin-orbit splitting ∼9.7 and 10.4 eV validates the existence of the trivalent state of Cr ion. Finally, the O-1*s* core-level spectra exhibit asymmetrical behavior, which is quite evident from the two-peak behavior because of surface absorbed oxygen species. These O-1*s* peaks are situated at 529.3 and 531.7 eV, in which the former one is due to the saturated O^{2-} ions, confirming the O-1*s* state. The presence of a secondary peak at 531 eV in the shoulder region can be ascribed to the surface-derived surplus of oxygen in the form of hydroxide (O-H) [27,28]. It is observed that the peak values exhibit a slight elevation in comparison with the theoretical ideal scenarios. However, the energy required for the electrons to transition from the 1*s* orbital to the unfilled 2*p* orbital is attributed to the binding energy of oxygen. The increase in binding energy is associated with the hybridization of the 2*p* orbital with the 1*s* orbital. No evidence of oxygen-metal bonds related to metal oxidation on the surface was detected [29,30].

C. Raman spectroscopy analysis

Now we move our focus to analyze distinct structural deviation of the orthorhombic *Pbnm* structure from the ideal cubic *Pm*-3*m* structure in terms of the Raman active modes. Generally, the *Pbnm* space group follows Glazer's notation $a^-b^+a^-$ tilt, which shows the mirror symmetry along the [010] plane and has three tilts, two of them with equal magnitude [31]. Figure 3 shows the Raman spectra recorded at room temperature in the wave number range $100 - 1000\,\mathrm{cm}^{-1}$ for three different systems GSO1, GSO5, and GSO9. For each spectrum, the Lorentzian functions are used to evaluate the exact peak position and the respective linewidths. Based on the *Pbnm* crystal symmetry, 24 Γ modes are active, arising at the Brillouin zone center in the primitive cell as given below:

$$\Gamma = 7A_{1g} + 7B_{1g} + 5B_{2g} + 5B_{3g}. \quad (3)$$

Here, A_{1g} and B_{1g} are the symmetric modes; two B_{2g} and two B_{3g} represent antisymmetric modes; one A_{1g}, two B_{2g}, and three B_{3g} correspond to bending modes; two A_{1g}, one B_{1g}, two

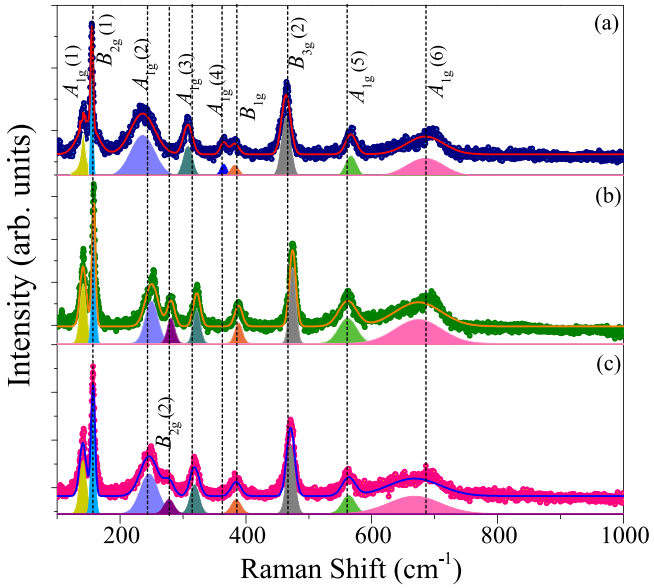

FIG. 3. The Raman spectra measured at room temperature (300 K) for all three compositions: (a) GSO1-blue (b) GSO5-green, and (c) GSO9-pink within the range of 100−1000 cm^{-1} along with the Lorentzian fittings corresponding to each spectrum. The nomenclatures of the individual modes are indexed based on appropriate spectroscopic term symbols.

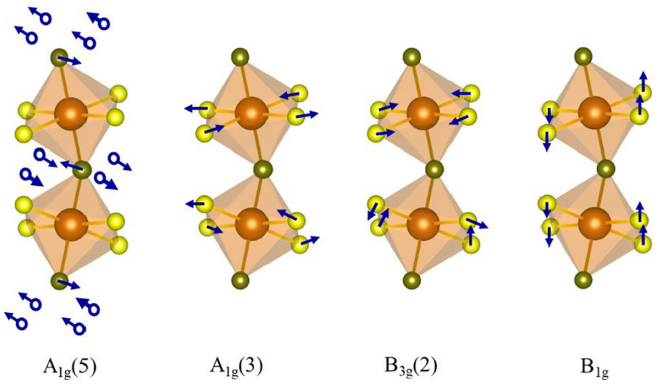

FIG. 4. The schematic of atomic vibration configurations of all four Raman active modes [$A_{1g}(5)$, $A_{1g}(3)$, $B_{3g}(2)$, and $B_{1g}(2)$]. These modes are listed here in order of decreasing frequency.

B_{2g}, one B_{3g} are rotational modes; and three A_{1g}, three B_{1g}, one B_{2g}, and one B_{3g} are arising due to the A-site cation displacement. The three main reasons for the appearance of the Raman active modes breaking the perfect cubic symmetry are (i) displacement of the A-site cation in the *Pm*-3*m* cubic structure, (ii) distortion of the transition metal oxide octahedra, and (iii) Jahn-Teller (JT) distortion [32]. In the present case, the first two clauses are associated with the center of the Raman activation, as Cr^{3+} is JT inactive. Among the above indexed 36 modes, few are optical and acoustic which are Raman inactive [33]. Overall, depending on the composition, we find a total of 10–11 modes detected exhibit blueshift and redshift for the respective modes, while the rest of the probable modes are not visible due to their low intensity [34–37]. All modes are indexed respectively and match well with the previously available literature; we compared our results appropriately, and these modes are listed in Table 2s in the Supplemental Material [21]. The schematics of some of the important modes are given in Fig. 4. The Raman mode shift is directly proportional to $\frac{1}{\sqrt{d}}$, with d as the bond length of the atoms, which is included and compared with the data given in Table 1s in the Supplemental Material [21]. The fluctuation occurring in each mode position moves toward the higher wave numbers upon decreasing the bond length. However, the modes at the lower wave numbers (within the range of 160 cm^{-1}) arise mainly due to the displacement of the A-site cations (Sm and Gd) in the perovskite lattice. The $A_{1g}(1)$ mode appears due to the movement of magnetic Gd^{3+} and Sm^{3+} cations along the z direction out-of-plane, whereas the $B_{2g}(1)$ phonon mode emerges due to the movement of cations at the A-site lying in the x direction. A shoulderlike anomaly is found ∼137 cm^{-1} for GSO1 and disappears for the other two compositions. The shoulderlike anomaly for GSO1 is not prominent, but for pristine compound $GdCrO_3$, the $B_{2g}(1)$ mode is more prominent due to the vibration of the Gd cation along the y direction. Because of the substitution of lighter-mass Sm at the Gd site, the vibration can get passive, and hence, that does not exist in the other two compositions where Sm concentration is higher. The same scenario was noticed in the case of the $B_{3g}(1)$ mode, which comes out as a result of the translation symmetry along the y direction, corresponding to the Gd^{3+} and Sm^{3+} cations [37]. The angular frequency (ω) is linked with the vibration of the atoms as $\omega \propto \sqrt{\frac{k}{m}}$, in which k is the force constant, and m is the reduced mass of the constituent atoms [36].

The substitution of lighter Sm (atomic mass: 150.36 u) at the Gd site (atomic mass: 157.25 u) shows a little change in the mode positions, especially the $A_{1g}(1)$ mode, which changes ∼2.2% in its position, as they tend to shift a little toward the lower wave numbers. This kind of displacement arises due to the vibrations which show little effect on the CrO_6 octahedral distortion. The next spectrum observed at 235 cm^{-1} arises due to the in-phase rotation of the CrO_6 octahedra along the y direction and is termed as the $A_{1g}(2)$ vibrational mode, which shifts ∼11 cm^{-1} for GSO5 as compared with the other two compositions. The $B_{2g}(2)$ mode ∼275 cm^{-1} is related to the Gd/Sm cation displacement in the Gd/Sm-O_{12} polyhedra along the z direction. As the larger-sized Sm ($r_{Sm} = 1.079$ Å) substitutes the Gd position ($r_{Gd} = 1.053$ Å), orthorhombicity gets reduced, resulting in the diminution of the mode intensity of GSO9, though the broad peak $A_{1g}(2)$ in Fig. 3(a) can be depicted as the combined effect of $A_{1g}(2)$ and $B_{2g}(2)$. The distance between the two modes gets more reduced in GSO5 than GSO1, so it can further merge or overlap together in the case of GSO9 finally leading a broad peak [37]. The $A_{1g}(3)$ mode of GSO9 occurring at ∼318 cm^{-1} shows a huge shift because of change in the Gd/Sm-O bond length in the opposite direction of the x axis of Gd/Sm-O_{12} polyhedra. The mode across 384 cm^{-1} is designated as an allowed symmetry crossover of $A_{1g}(4)$ and B_{1g} modes originating from out-of-phase rotation of CrO_6 octahedra in the x direction, while the Gd/Sm-O stretching and antistretching movement takes place along the z direction. In the case of the GSO9 system, the evolution of the two

prominent peaks finally merges and shows a similar spectrum to that of GSO5 and GSO1 (with increasing the R-site cationic radius). The $B_{3g}(2)$ mode at $\sim$470 cm^{-1} is insensitive toward the orthorhombic distortion which occurs due to the out-of-phase bending or stretching of the CrO_6 octahedra [37]. This mode maintains a sharp intensity with a little shift in position (1.2%). The prominent and broad peak fixed at $\sim$563 cm^{-1} is labeled $A_{1g}(5)$, arising from the antisymmetric stretching of the CrO_6 octahedra [35]. In the present case, a broad phonon mode within the range of 660 – 690 cm^{-1} can also be noticed for the Sm-substituted systems contrary to the pristine compositions $GdCrO_3$ and $SmCrO_3$ [36]. This feature indicates the complex mixture of atomic distortion and defects caused by the two cations at the A-site, which is denoted by the $A_{1g}(6)$ mode. All parameters obtained after the mathematical fitting of this mode have been listed in Table 3s in the Supplemental Material [21]. Based on previous research, it can be inferred that the observed mode deviation is caused by the local breathing mode of oxygen. This mode is primarily a result of the charge transfer occurring between the unpaired *d* and *f* orbitals of rare-earth cations and the unfilled *p* orbitals of adjacent oxygen ions [38]. Interestingly, the addition of Sm^{3+} at the Gd^{3+} site reflects the change in the intensity and sharpness [full width at half maximum (FWHM)] of the Raman spectrum which clearly refers to the structural deformation (tolerance factor) of the system.

1. Temperature-dependent Raman analysis

A comprehensive investigation was conducted to establish a correlation between the magnetic transitions and the origin of Raman active modes. This involves conducting a meticulous temperature-dependent Raman measurement within the wave number range of 100 – 800 cm^{-1}, spanning temperatures from 80 to 300 K. The prominent observations as a result of anharmonicity of the primitive cell lattice dynamics are realized by means of (a) the lower wave number modes intensify when the measurement temperature approaches T_N ($\sim$196 K) and start getting diminished as the temperature reaches 113 K, thereafter, maintaining a similar intensity variation at low temperatures. (b) The sharpness of the modes of higher wave numbers decreases significantly (FWHM increases), while the lower wave number modes become sharper as the temperature approaches T_N and start getting broader for $T < T_N$. No structural phase transition was observed in the investigated temperature and wave number range. To precisely obtain the Raman peak position, FWHM, intensity, and the deconvoluted spectrum using Lorentzian profiles at each individual temperature, we followed the Granado *et al.* [39] mathematical relation as given below:

$$\omega(T) = \omega_0(T) + \Delta\,\omega_{\text{lat}} + \Delta\omega_{\text{s-ph}} + \Delta\omega_{\text{el-ph}} + \Delta\omega_{\text{anh}}. \quad (4)$$

In the above expression, $\omega_0(T)$ is the frequency of the corresponding mode at absolute temperature in the harmonic approximation. The second term represents the frequency at which the lattice undergoes expansion or contraction due to variations in the ionic binding energy, and this feature is commonly observed in isotopically expanded systems. Here, $\Delta\omega_{\text{s-ph}}$ represents the deviation of phonon frequency of spin-lattice coupling because of the phonon modulation of the spin-exchange integral. The fourth term elucidates the effect of a renormalization of the electronic states of the constituent elements and can be neglected for low carrier concentration. The last term signifies the change in the intrinsic anharmonic frequency at constant volume, which is formulated as follows [40]:

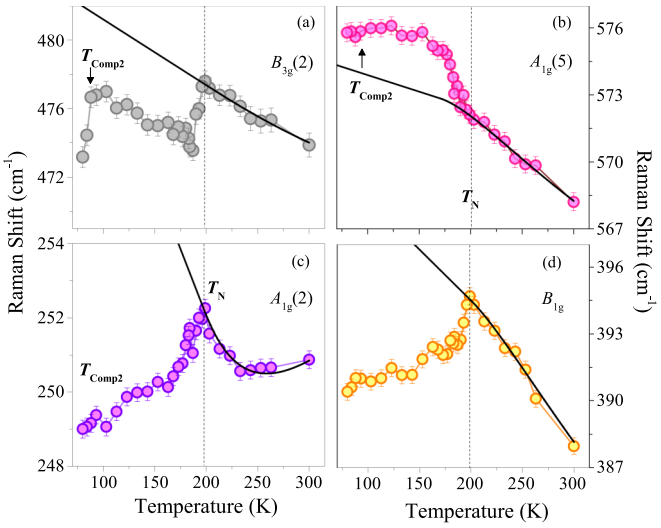

FIG. 5. The thermal evolution of the Raman shifts of GSO5 for some of the selected Raman modes: (a) $B_{3g}(2)$, (b) $A_{1g}(5)$, (c) $A_{1g}(2)$, and (d) B_{1g} in the temperature window 80–300 K. The solid black lines represent the fitted curves of frequency dependence of anharmonic phonon-phonon scattering according to Eq. (5). The vertical dashed lines are visual guides corresponding to T_N. The respective modes clearly show the anharmonic nature at lower temperatures.

$$\omega_{\text{anh}}(T) = \omega_0 + A\left(1 + \frac{2}{\frac{\hbar\omega_0}{e^{2k_BT}-1}}\right) + B\left[1 + \frac{3}{\frac{\hbar\omega_0}{e^{3k_BT}-1}} + \frac{3}{\frac{\hbar\omega_0}{(e^{3k_BT}-1)^2}}\right]. \quad (5)$$

Here, *A* and *B* are the anharmonic coefficients obtained from the Raman data fitting above T_N. The detailed thermal response of some of the specified phonon modes, namely, $B_{3g}(2)$, $A_{1g}(5)$, $A_{1g}(2)$, and B_{1g}, are depicted in Figs. 5(a)–5(d), respectively, within the temperature range 80–300 K. All modes show gradual softening or hardening with fixed anomaly at T_N. However, the mode $B_{3g}(2)$ exhibits a hardening nature below T_N, like the previous reports on the $YCrO_3$ polycrystalline sample, which are related to the relaxing of the CrO_6 octahedra [41]. The out-of-phase rotation of the octahedra associated with B_{1g} fitted with Eq. (2) shows a prominent softening at lower temperature with the deviation from the anharmonicity, indicating the presence of another factor, possibly direct spin-phonon coupling. The hardening of antisymmetric stretching mode $A_{1g}(5)$ can be understood because of the exchange-striction effect and the presence of Cr^{3+}-Cr^{3+} AFM coupling. In $GdCrO_3$, this mode hardening is consistent with the cell volume reduction, indicating a strong spin-phonon coupling of Gd^{3+}-Cr^{3+} interaction [35]. The softening of in-phase rotation of the CrO_6-octahedra-driven

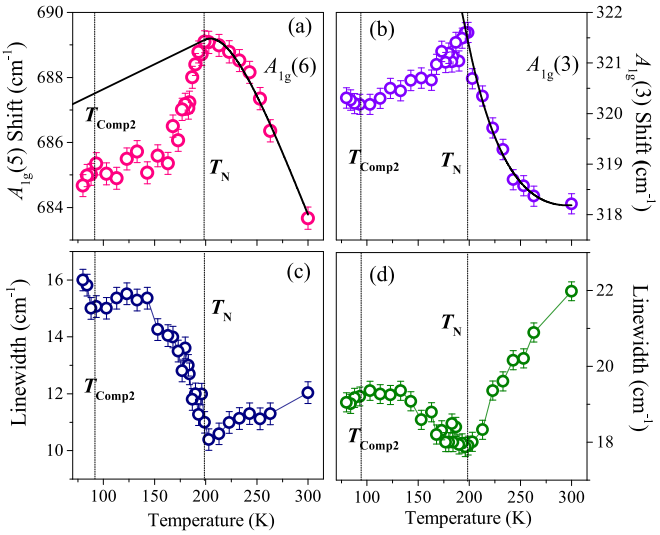

FIG. 6. The temperature dependence of Raman modes (a) $A_{1g}(6)$ and (b) $A_{1g}(3)$ within the temperature range of 80–300 K in the top panel. The corresponding linewidths are plotted in the bottom panel. The scattered symbols are the data points along with frequency error bars. The solid black line is the fitted curve with Eq. (5). The dotted lines are the visual guides representing the location of T_N and T_{Comp2}.

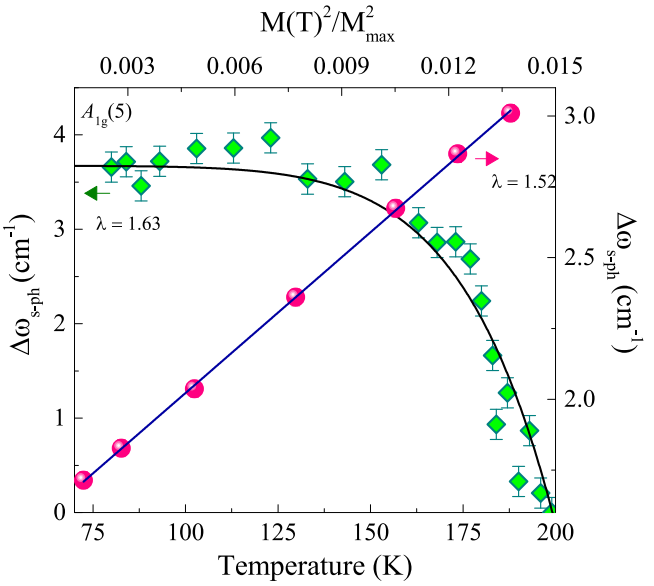

FIG. 7. The thermal dependence of $\Delta\omega_{s\text{-}ph}$ corresponds to the $A_{1g}(5)$ mode in the left-hand side scale (green diamond symbols) with the black solid curve representing the best fit of Eq. (8a). The right-hand scale represents the variation of $\Delta\omega_{s\text{-}ph}$ with respect to $[M(T)/M_{max}]^2$ (corresponds to the pink spheres) and the navy blue line is the fitted curve with Eq. (8b). The direct correlation between phonon instability and magnetic characteristics with the help of chosen mode $A_{1g}(5)$ has been confirmed.

$A_{1g}(2)$ below the transition temperature is consistent with the previous results [42]. Such softening can be ascribed to the quasiharmonic effect and thus could be related to the change in the tilt angles (θ_1 and θ_2) arising due to the Gd^{3+}-Cr^{3+} exchange interaction [42]. Figure 6 demonstrates the thermal evolution of $A_{1g}(6)$ and $A_{1g}(3)$ modes. The softening of the $A_{1g}(6)$ mode by ∼0.5% toward liquid nitrogen temperature happens because of Cr^{3+} ordering due to the magnetostriction effect. However, it should be noted that the FWHM is related to the phonon lifetime, which usually alters with measurement temperature. From Fig. 6(c), the inconsistency around the same temperature precluded the magnetostriction effect present in the system, implying the existence of direct spin-phonon coupling. Previously, Sarkar *et al.* [36] reported higher oxidation state of Cr (+5, +6) as the origin of this mode, but the XPS analysis of the Cr-cation oxidation state ruled out that possibility. The intense softening of the $A_{1g}(3)$ mode down to transition shows a similar anomaly in the linewidth as well [Fig. 6(d)], which refers to the influence of Gd^{3+}-Cr^{3+} spin-phonon coupling on the A-site cation (Gd/Sm) movement in the Gd/Sm-O_{12} polyhedra [35]. The atypical characteristics of the Raman spectrum of deviation of this frequency from its intrinsic nature is related to the renormalization of the phonon modes due to the corresponding magnetic transition. This shift can be written in the form:

$$\Delta\omega_{s\text{-}ph} = \omega(T) - \omega_0 = \lambda\langle \boldsymbol{S_i}\, \boldsymbol{S_j}\rangle, \tag{6}$$

where $\omega(T)$ symbolizes the renormalized phonon frequency at a particular temperature, and λ represents the spin-phonon coupling constant, which depends on the change in the bond length and bond angle between the atoms concerning oxygen atoms. The spin-spin correlation function $\langle \boldsymbol{S_i}\, \boldsymbol{S_j}\rangle$ denotes the average of the nearest neighbor i^{th} and j^{th} site spin interaction [39]. Now from the molecular field theory approximation, the spin-spin correlation function can be written as

$$\langle S_i\, S_j\rangle \approx 4\left[\frac{M\,(T)}{4\mu_B}\right]^2, \tag{7}$$

where $M(T)$ is the magnetization of the FM contribution coming from the transition metal ions. Thus, finally inserting Eq. (7) into Eq. (6), thermal dependence of the frequency mode arising due to the spin-phonon coupling can be simplified into

$$\Delta\omega_{s\text{-}ph} \approx \lambda S^2\left[1 - \left(\frac{T}{T_N}\right)^{\gamma}\right], \tag{8a}$$

$$\approx \lambda\left[\frac{M(T)}{M_{sat}}\right]^2, \tag{8b}$$

where $S = \frac{3}{2}$, and M_{sat} is the saturation magnetization of the corresponding system [35]. Here, the $A_{1g}(5)$ mode is analyzed, as it shows prominent deviation from the ideal anharmonic nature and follows a trend as shown in Fig. 7. Here, thermal dependence of $\Delta\omega_{s-ph}$ (green diamond symbols) along with the fitted curve (with Eq. (8a)) is shown in Fig. 7. Here the black line on the left-hand-side scale shows the best fit corresponding to the Eq. (8a). While the variation of $\Delta\omega_{s-ph}$ according to Eq. (8b) is shown by the pink spheres and the navy blue line represents the linear fit. Here, the coexistence of both positive and negative shifts is the result of the competitive interaction of canted AFM and FM correlations below the Néel temperature. Following this, Eq. (6) can be written in the form of lattice vibration force constants k_1 and

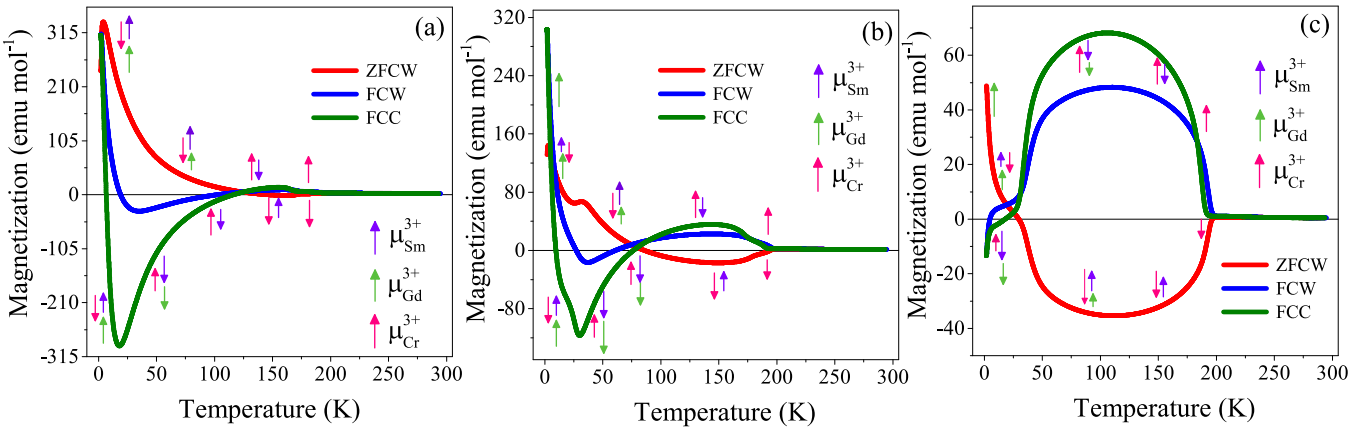

FIG. 8. The temperature dependence of three different magnetizations $M(T)$ measured under various protocols zero-field cooled (ZFC), field-cooled cooling (FCC), and field-cooled warming (FCW) for (a) GSO1 (b) GSO5, and (c) GSO9 for an external field of $H_{DC} = 100$ Oe. The respective spins of Sm^{3+}, Gd^{3+}, and Cr^{3+} are designated by purple, green, and red lines, respectively. The high-temperature compensation temperature and multiple magnetic crossovers are obvious in all three compositions.

k_2 as

$$\Delta\omega_{\text{s-ph}} \propto -k_1\langle \boldsymbol{S_i S_j}\rangle + k_2\langle \boldsymbol{S_i S_k}\rangle, \tag{9}$$

with the assumption of k_1 and k_2 corresponding to the FM and canted AFM exchange interactions between the nearest spins $\langle \boldsymbol{S_i S_j}\rangle$ and $\langle \boldsymbol{S_i S_k}\rangle$, respectively, which depend on the temperature. The magnitude of $(k_2 - k_1)$ indicates the polarity of the phonon mode shift [41]. In Fig. 7, the excellent fit of experimental data with the above expressions represents the domination of nearest-neighbor Cr^{3+}-Cr^{3+} antisymmetric exchange interaction. The symmetric exchange coupling constant (J_e) is an order higher in magnitude than that of the antisymmetric one (D; see Table 2s in the Supplemental Material [21]). The values of the spin-phonon coupling constant from magnetization data ($\lambda \sim 1.52$) match well with that obtained from the order parameter ($\lambda \sim 1.63$) and with the previous reported data [35]. These results corroborate the existence of strong magnetoelectric coupling present in the system, as evidenced by the dielectric measurement and the enhancement of polarization with magnetic field reported previously [35].

IV. MAGNETIC STRUCTURE

A. Temperature dependence of magnetization

In Fig. 8, we show the temperature dependence of the DC magnetization $M(T)$ measured under conditions such as ZFCW, FCC, and FCW protocols in the presence of external applied field of $H_{DC} = 100$ Oe for all three investigated system. Here, $M(T)$ behavior of the GSO1 system depicted in Fig. 8(a) shows a robust AFM ordering with Néel temperature $T_N = 196$ K. Upon further decrease of temperature, the magnetization increases as measured under the FCC protocol. Beyond $T_{\text{Bifurcation}} = 157$ K, the magnetization value decreases, corresponding to the change of the slope [Fig. 8(a)], and the net magnetization M_{Net} becomes zero at $T_{\text{Comp1}} = 116$ K, which finally exhibits large negative magnetization. After attaining the maximum negative magnetization (~ -294 emu/mol) at 19 K, the magnetic moment increases ($+M$) further, and $\sim$6.7 K, a significant zero-crossover was evident in M_{FCC}, although M_{FCW} crosses the null point at slightly higher temperatures $\sim$19 K. Overall, now we call this point the second compensation point ($T_{\text{Comp2}} = 6.7$ K). Interestingly, both M_{FCC} and M_{FCW} increase monotonously until 2 K. However, $M_{\text{ZFCW}}(T)$ shows the clear role of trivalent Gd spins, which gets order across 9.3 K, commonly referred to as spin-reorientation temperature ($T_{\text{SR}} = 9.3$ K), yet at higher temperatures, M_{ZFCW} gradually decreases its magnitude until 145 K, where the system goes through the zero-crossover of magnetization and gradually decreases its value as the temperature approaches T_N.

For GSO9 [Fig. 8(c)], the $M(T)$ variation shows an entirely different trend in which the magnetization switches its polarity at 29.8 K (T_{Comp1}) upon heating from 2 K, reaches a maximum negative magnetization at 111 K. The magnetization slowly increases until 196.5 K (T_{Comp2}) and the system becomes paramagnetic beyond T_N. Both FCC and FCW magnetization increase below T_N with significant hysteresis between them until 27 K and cross the zero-magnetization axis at 18 K (T_{Comp1}). On the other hand, $M(T)$ of GSO5 exhibits a similar trend as GSO1 with slight change in the ordering temperatures, as evident from Fig. 8(b). Significant enhancement in T_N (193.7 K) was noticed in this composition as compared with the other two systems GSO9 and GSO1, in which the polarity of magnetization changes nearly twice measured under all three protocols. Here, the hysteresis between FCC and FCW becomes smaller in both temperature ranges, and the magnetic moment with a crossover across 76 K (T_{Comp2}), which attains a maximum negative magnetization (-116.6 emu/mol at 30 K) for M_{FCC}, shows a positive magnetization after 9.7 K (T_{Comp1}). The DC magnetization under the ZFCW protocol shows a spin flip at 29 K (T_{SF}) and slowly reaches T_{Comp1} at 181.3 K followed by T_N. The arrows of pink, green, and violet depict the spins of Cr^{3+}, Gd^{3+}, and Sm^{3+}, respectively.

After discussing different magnetic transitions and their trend/magnitudes, now we focus on the role of different cations in deciding their global magnetic behavior. In the present case, the magnetic ordering is completely dominated by the coexistence of the competing multiple exchange

interaction between the cations present in the system: Cr^{3+}-Cr^{3+}, Gd^{3+}-Gd^{3+}, and Gd^{3+}-Cr^{3+}. The structural and magnetic unit cells are equivalent for rare-earth orthochromite oxides ($RCrO_3$) with the Wyckoff positions 4*b* for Cr $(\frac{1}{2}, 0, 0)$, $(\frac{1}{2}, 0, \frac{1}{2})$, $(0, \frac{1}{2}, \frac{1}{2})$, and $(0, \frac{1}{2}, 0)$. The first magnetic transition starting from room temperature is T_N, which is attributed to the ordering of the Cr^{3+} sublattice in *G*-type AFM configuration along with the weak FM component, which is explained based on the Dzyaloshinskii-Moriya (DM) exchange mechanism [43]. At T_N, the rare-earth Sm^{3+} and Gd^{3+} moments are in disordered configuration. According to Bertaut [44], the magnetic unit cell orders with the propagation vector $k = 0$, maintaining the Γ_4 (G_x, A_y, F_z) configuration intact. The Γ_4 configuration carries an uncompensated FM component oriented parallel to the z crystallographic axis with Cr spins oriented along the DC field for M_{FC} and opposite to it under the M_{ZFC} condition. Upon lowering the temperature to 161 K (185 K) for GSO1 (GSO5), the FC and ZFCW curves start to deviate opposite to each other, which is represented as $T_{Bifurcation}$. Structural or magnetic phase transitions are absent here; however, only the Cr^{3+} spins start to get aligned and create an internal field on the rare-earth sublattices. The temperature range corresponding to this region is negligible for GSO9. Further, on decreasing the temperature, the rare-earth Sm^{3+} spins slowly start to polarize themselves antiferromagnetically with the internal field of the Cr^{3+} sublattice aligning opposite to the Cr^{3+} spins. The GSO1 system experiences a fully compensated sublattice magnetization of competing Cr and Sm (and some Gd) moments at $T_{Comp1} \sim 145$ K, and the compensation shifts to lower temperatures for GSO5 (∼75 K) as more Sm^{3+} moments persist to hold the uncompensated Cr^{3+} spins back to AFM configuration toward the x axis. For GSO9, the antiparallel spins of Gd^{3+} and Sm^{3+} causes the magnetization to reach its maximum negative value across (T_{Min}) below which a change in slope occurs across $T_{SR} \sim 37$ K.

Gorodetsky *et al.* [20] reported that the spin-reorientation transition at T_{SR} could be a continuous process which is second order in nature, where the AFM Cr^{3+} spins rotate to align in Γ_2 (F_x, C_y, G_z) spin orientation. This feature manages to persist in GSO5 at lower temperatures (28 K) as the smaller numbers of Sm^{3+} moments are not enough to rotate the Cr^{3+} spins from the z to the x crystallographic axis at higher temperatures. For Gd-rich system (i.e., GSO1 in the present case), the anomaly at 9.3 K is due to the continuous rotation of uncompensated Gd spins from the z to the x axis driven by Gd^{3+}-Cr^{3+} anisotropic exchange interaction, which is designated as T_{SR} or T_N^{Gd}, that occurs at lower temperature (∼5.8 K for GSO5). The sharp change in slope of $M(T)$ ∼28.3 K (labeled T_{SF}) is noticeable in GSO1 and GSO5 in both M_{FCC} and M_{FCW} protocols.

The flipping of the Cr^{3+} spins and both rare-earth spins can be explained using the Zeeman energy: $E_{Zeeman} = -\mu_0 M_{Net} H_{DC} \cos\theta$, where μ_0 is the permeability of free space, M_{Net} is the net resultant moment of Cr^{3+} and B-site cations (Sm^{3+} and Gd^{3+}) of a primitive magnetic cell, and θ is the angle between M_{Net} and H_{DC}. Here, the angle θ changes from $\theta = \pi$ to $\theta = 0$ as E_{Zeeman} changes from positive to negative with lowering of the temperature. In the case of $M_{FCW}(T)$, the region becomes a little broader than $M_{FCC}(T)$ as spins flip from stabile zone which takes more thermal

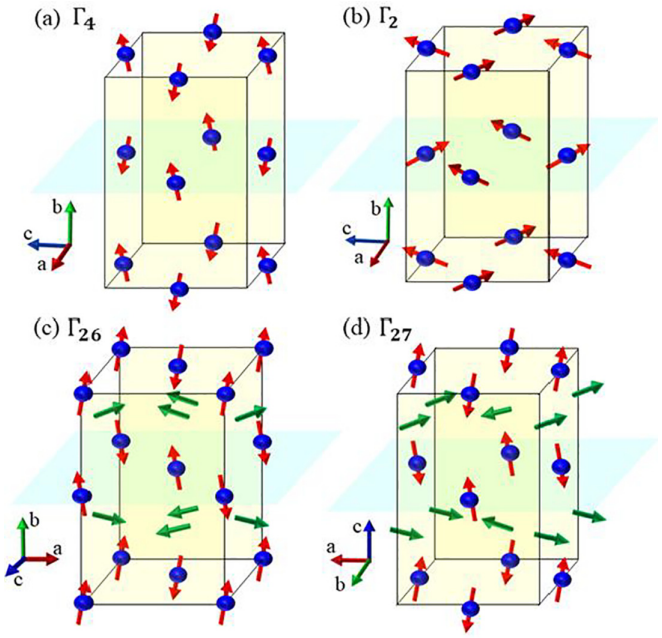

FIG. 9. Different possible spin configurations of the perovskites (Gd,Sm)CrO_3 within *Pbnm* symmetry (*a*) Γ_2, (b) Γ_4, (c) Γ_{26}, and (d) Γ_{27} with the arrows symbolizing the spins.

energy. Hereafter, the magnetization increases due to activation of high trivalent Gd moment (of ∼7.94 μ_B) with lowering the temperature, finally leading M_{Net} to be zero (at T_{Comp2}) ∼7 K (9.7 K) for GSO1 (GSO5), where the combined magnetization of Cr^{3+} and AFM-ordered Gd^{3+}-Sm^{3+} along the x axis counterpoises each other. For Sm-rich GSO9, the large hysteresis between FCC and FCW starting from T_N to $T \sim 30$ K is the indication of disordered mixed phase magnetic regions having glassy arrested spin states termed magnetic glass (T_{MG}) [18]. Cooling the system through T_{SR} induces the arrested metastable state which is AFM insulating in nature, with the onset of frozen kinetic motion becoming more pronounced across T_{MG}. This situation persists until the temperature reaches a sufficiently low level, referred to as the supercooled state, at which point the trivalent Sm and Gd spins become fully activated and align themselves with the internal induced field [45]. The discernible reduction after T_{Comp1} for GSO9 ∼6.8 K (T_{Sm}) is the result of the advent of the exchange interaction between Sm^{3+}-Sm^{3+}, which orders antiferromagnetically around the second-order phase transition. This extra magnetic ordering is due to the orientation of polar phase either to Γ_{26} $(C_x, G_y, C_x; C_x^R, A_y^R, F_z^R)$ or Γ_{27} $(F_x, C_y, G_z; F_x^R, C_y^R, G_z^R)$ [11]. We present all these features more specifically in Fig. 9 where several possible spin configurations of the investigated system within the *Pbnm* symmetry are shown. In particular, the magnetic phases Γ_{26} $(C_x, G_y, C_x; C_x^R, A_y^R, F_z^R)$ or Γ_{27} $(F_x, C_y, G_z; F_x^R, C_y^R, G_z^R)$ are clearly represented in this figure with specific directions of spin represented through the arrows.

Figures 10(a) and 10(b) depict the temperature dependence of the first derivative of (χT) for $H_{DC} = 100$ Oe. The magnitude of (χT) signifies the magnetic energy associated

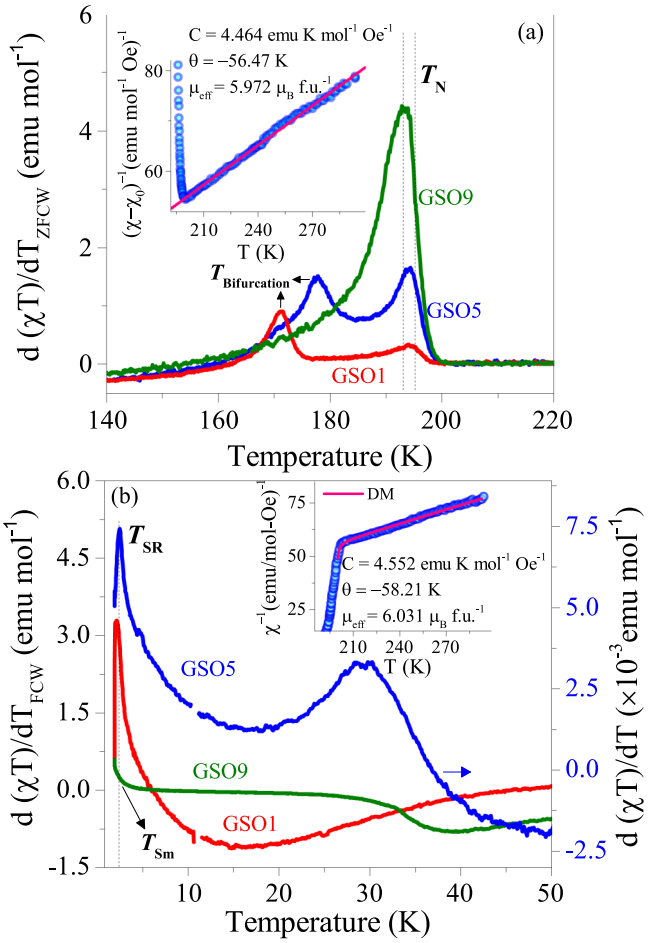

FIG. 10. The temperature derivative of the magnetic susceptibility (χT) plots for GSO1 (red), GSO5 (blue), and GSO9 (green) measured under (a) zero-field-cooled warming (ZFCW) and (b) field-cooled warming (FCW) protocols along with the Curie-Weiss fit and modified Curie-Weiss fit considering the antisymmetric Dzyaloshinskii-Moriya (DM) interactions as shown in the insets of (a) and (b), respectively.

with the magnetic unit cell, and the temperature derivative denotes the exact location of the AFM-to-paramagnetic phase transition region (T_N) and T_{SR}. From Fig. 10(a) one can clearly notice a minor change in the ordering temperatures (depicted with the dotted vertical lines) of all the three investigated systems (GSO1) to 194 K (GSO9) which agrees well with the values obtained from *M-T* curves with the increment of the magnetic moment of ∼92.7%, as discussed above. The presence of an additional peak at lower temperatures, specifically ∼171 K (GSO1) and 177.8 K (GSO5), indicates a change in slope of differential susceptibility. This change in slope follows a similar pattern as the transition temperature (T_N), which shifts toward higher temperatures as the concentration of Sm increases. It is noteworthy that this feature is not present in GSO9. The calculated value of effective moment (μ_{eff}) of GSO5 is 6.845 μ_B /f. u., and here, the temperature-independent diamagnetic susceptibility term (χ_0) has been subtracted from the current experimental values in which the magnitude of χ_0 was obtained from the nonrelativistic Hartree-Fock calculations performed by Mendelsohn *et al.* [46]. To estimate μ_{eff}, the inverse susceptibility data (for $T > T_N$) have been plotted and fitted with the Curie-Weiss (CW) law: $\chi^{-1} = \frac{T-\theta_{CW}}{C}$, as shown in the inset of Fig. 10(a). Here, θ is the Weiss temperature, and C is the Curie constant. This analysis yields $\mu_{eff} = 5.97\ \mu_B$ /f. u., and the other parameters are tabulated in Table 4s in the Supplemental Material [21]. Figure 10(b) describes the thermal variation of T_{SR} as it changes from 2.23 K (for GSO1) to 2.46 K (for GSO5). We employed the DM interaction in the present case as the contribution of the weak FM component along the z crystallographic axis. Accounting for the DM exchange interaction, the average susceptibility data deviate from the linear behavior in the vicinity of T_N [47]. The inset in Fig. 10(b) shows the inverse susceptibility fitted with the DM modified CW law $\chi^{-1} = \frac{(T-\theta_{CW})\,(T-T_N)}{C(T-T_0)}$, where T_0 and T_N are the characteristic parameters extracted from the fits. Here, we find that the perpendicular contribution is dominant for the average susceptibility $\chi_{Avg} = \frac{\chi_{||}+2\chi_{\perp}}{3}$ for the G_xF_z-type canted AFM system. The symmetric (J_e) and antisymmetric (D) exchange interactions occupying Cr^{3+} moments can be evaluated using the semiquantitative analysis reported in previous studies [28], and the evaluated parameters are listed in Table 2s in the Supplemental Material [21]. The observed correlation between the increasing J_e and the increase of Sm content is consistent with the corresponding increase in the value of T_N. In the preceding section, it was determined that, in addition to the prevailing canted AFM behavior exhibited by Cr^{3+}, there exists a secondary, less prominent FM component (M_{Cr}) that imparts an internal field (H_{int}) on the rare-earth cations. Consequently, as the temperature decreases below T_N, the rare-earth cationic moments (M_{Sm} and M_{Gd}) exhibit AFM alignment from their initial paramagnetic state, transitioning from their initial paramagnetic alignment. This causes the negative magnetization of $|M_{Cr}| = |M_{Sm/Gd}|$. The magnitude and polarity of the induced H_{int} have been obtained by fitting the phenomenological relation given by Cooke *et al.* [48] under applied field of H_{app} within the range of 40–150 K:

$$M = M_{Cr} + C_{Gd}\frac{(H_{int} + H_{app})}{(T-\theta)}, \tag{10}$$

where C_{Gd} is the Curie constant of the Gd^{3+} ion. The C_{Gd} of the ground state at 7.87 emu K/Oe mol obtained analytically [19] has been kept fixed during the fitting process. The fitted data are displayed in Fig. 11 with H_{app} of 100 Oe for both FCC and FCW curves, and the obtained parameters are listed in Table 4s in the Supplemental Material [21]. The fitting procedure is exclusively performed for the FCC case of GSO9, as the magnetization does not attain negative values for FCW. The negative magnetization is observed to persist up to H_{app} of 400 Oe for GSO1 and GSO5 (data not presented). Beyond this threshold, the magnetic field becomes sufficiently strong to overcome the induced internal magnetic field of Cr^{3+}, resulting in an increase in the positive magnetization. The negative value of H_{int} indicates the antialignment of Cr spins with respect to H_{app}. The magnetic moment M_{Cr} is found to increase rapidly in both FCC and FCW cases upon increasing the Sm content from GSO1 to GSO9, indicating dominant contribution of the FM component of Cr^{3+}, which aligns toward the rare-earth cations. The value of H_{int} increases

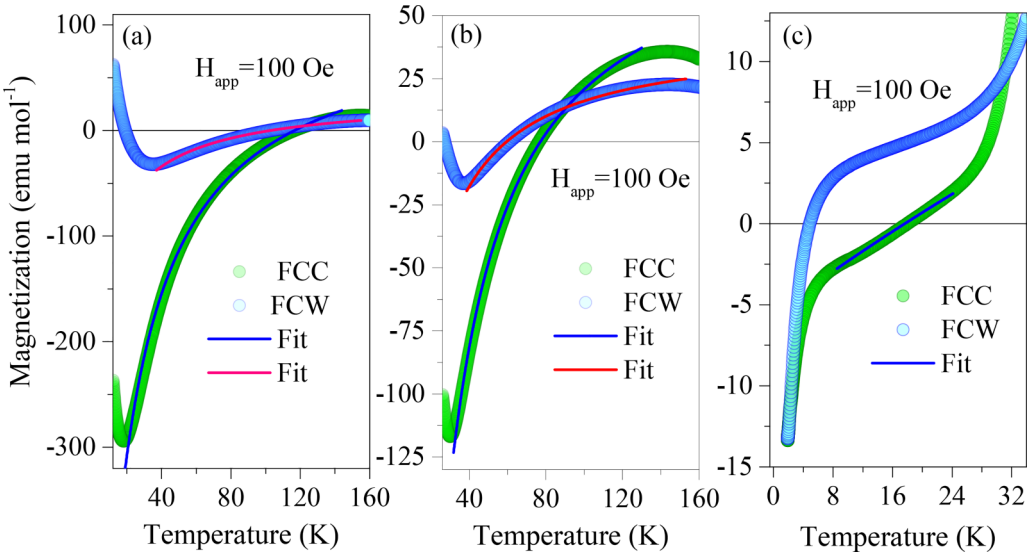

FIG. 11. The temperature variation of field-cooled warming (FCW; blue) and field-cooled cooling (FCC; green) magnetization curves of GSO1, GSO5, and GSO9 samples, respectively, from the left. The solid lines represent the mathematical fits corresponding to Eq. (10), $M = M_{\mathrm{Cr,Sm}} + C_{\mathrm{Gd}} \frac{(H_{\mathrm{int}} + H_{\mathrm{app}})}{(T-\theta)}$. H_{int} leads the origin of negative magnetization affecting the individual magnetization of rare-earth sublattices.

from −2123 Oe (GSO1) to −5321 Oe (GSO9) for the FCC protocol, indicating the requirement of higher field to polarize the rare-earth moments by H_{int} [49].

B. Disordered magnetic phases: Magnetic glasslike arrest of kinetics

The magnetic glasslike state typically manifests when an external magnetic field is present, exhibiting distinct characteristics from the commonly recognized metastable state known as the spin-glass state. The glassy signature is typically observed in crystalline solids that exhibit nonequilibrium clusters of frozen FM and AFM spin structures, which are influenced by the thermomagnetic history [13]. The decelerated relaxation of the magnetic phase transition can be attributed to the delayed initiation and expansion of the supercooled AFM phase. The substantial disparity observed in the magnetization curves of GSO9 between the FCC and FCW configurations signifies the presence of thermomagnetic irreversibility, which plays a notable role in the phenomenon of phase coexistence [13]. For FCC, T_{SR} is assigned to the Γ_4-to-Γ_2 second-order phase transition, where the reverse (Γ_2 to Γ_4) occurs during the FCW protocol because of the Sm^{3+}-Cr^{3+} exchange interaction, as precluded in the previous section. The thermomagnetic irreversibility assists the higher volume fraction of the FM phase obtained in FCC than that of FCW in the range of 180–30 K and relates to the higher magnetic moment of FCC than FCW. In other words, gradual thermal hysteresis within the range of 190–25 K and multiple crossovers between FCC and FCW occur due to the kinetic arrest of the FM-to-AFM transition, signifying magnetic glass behavior. The scattered islands of the FM matrix in the AFM background (FCW), and vice versa under FCC, in the vicinity of T_{SR} hinders the second-order phase transition, leading to the nonequilibrium magnetic glass state [50].

In the proximity of the spin-reorientation transition, the anisotropic exchange interaction between Sm^{3+} and Cr^{3+} results in an induced field that imparts distinct polarizations of positive and negative fields on the up and down spins of Cr^{3+}. This effect becomes more pronounced as the temperature decreases, as the activation of the rare-earth Sm^{3+} moments (and Gd^{3+} at significantly lower temperatures) intensifies [20]. On overcoming the crystalline barrier anisotropy, the effective field rotates the spins along the crystallographic axis parallel to the y direction, leading the spin reorientation [51]. The characteristic magnetic glass behavior is thus investigated with the temperature sweeps under different cooling and warming protocols in the phase transition regime, as shown in Fig. 12. The limitation of the cooling temperature is kept here with the applied field ∼100 Oe. The investigated sample is cooled from room temperature at 300 K to 30 K under the field bias of $H_{\mathrm{DC}} = 100$ Oe, followed by a hold time of 100 s. Subsequently, the sample has been warmed until 40 K with the slow sweep rate and again cooled until 27 K, followed by warming up to 40 K. Finally, it was cooled again until 27 K with the same sweep rate, followed by gradual warming until 300 K. The FCC magnetization appears higher in magnitude than that of FCW. During the cooling protocol, the large anisotropy of Cr^{3+} holds some of the FM clusters, contributing to the AFM-dominant Γ_4 phase in the supercooled condition in the vicinity of T_{SR}. This mixed phase of both Γ_4 and Γ_2 is metastable and gives rise to the frozen glassy nature (T_{MG}). With further reduction in temperature below T_{MG}, the energy involved with the Sm^{3+}-Cr^{3+} exchange interaction overcomes the anisotropy energy, and most of the spins inherit Γ_2 configuration with higher energy values by slowly rotating throughout all the infinitesimal angles [51]. For the FCW protocol, during the transforming process, a small number of spins with Γ_2 configuration stays like islands in the majority Γ_4 phase due to the relatively smaller Sm^{3+}/Gd^{3+} anisotropy. Hence, the system seeks equilibrium, trying to maintain the lower-energy AFM phase, lowering the magnetization in the warming protocol [50]. The magnetization difference between

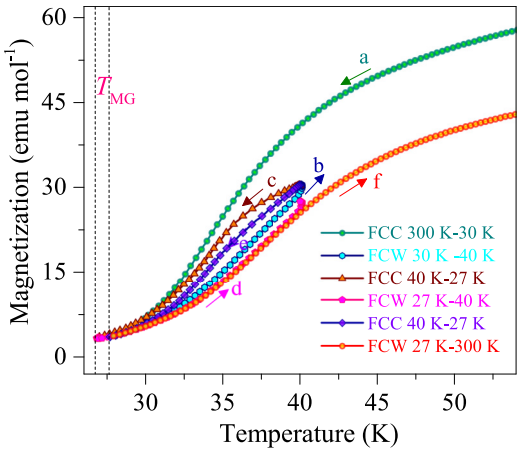

FIG. 12. The cycling M-H loops within the magnetic glasslike transition temperature, where the sample is taken to room temperature with the presence of 100 Oe external field [field-cooled warming (FCW)], then cooled to 30 K [field-cooled cooling (FCC)], further warmed until 40 K (FCW), cooled to 27 K (FCC), warmed to 40 K (FCW), again cooled to 27 K (FCC), and finally warmed until room temperature (FCW). The very existence of the frozen magnetic glasslike characteristics have been confirmed.

the FCW and FCC protocols, i.e., M_{FCC}-M_{FCW}, defined as M_X is shown in Fig. 13(a) to understand the phase fraction of FM/AFM components. The increment of the field from 100 to 1000 Oe diminishes the divergence of the magnetization difference within the range of 60–185 K. The maximum of $M_X(T)$ can be observed at ∼105 K for $H_{DC} = 100$ Oe and increases to 113 K for higher fields of 400 and 1000 Oe. It is interesting to note that the glassy nature exists at 1000 Oe. Further, we predict that the higher-field $H_{DC} > 1000$ Oe can slowly demolish the frozen state, as the greater number of FM spins will be aligned in the FCW mode leading to diminishing of difference between the magnetization measured under heating and cooling conditions [50]. It was previously reported that the thermomagnetic irreversibility depends strongly on the phase fraction δ, defined as the ratio of the AFM/FM phase in the FCW protocol and vice versa in the FCC magnetization,

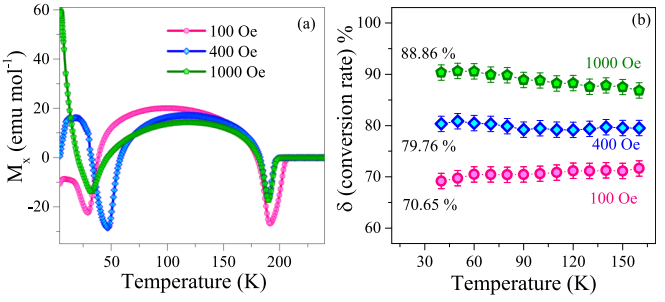

FIG. 13. (a) The transformation of $M_X(=M_{FCC}$-$M_{FCW})$ with respect to temperature of GSO9 under specified $H_{DC} = 100$ Oe (pink), 400 Oe (blue), and 1000 Oe (green). (b) The temperature dependence of conversion factor $\delta(T)$ ($\delta = M_{FCW}/M_{FCC}$) for three different fields (100, 400, and 1000 Oe) within the temperature range of 40–160 K. The frozen state can be realized with the help of phase fraction of ferromagnetic (FM) clusters over antiferromagnetic (AFM) spins.

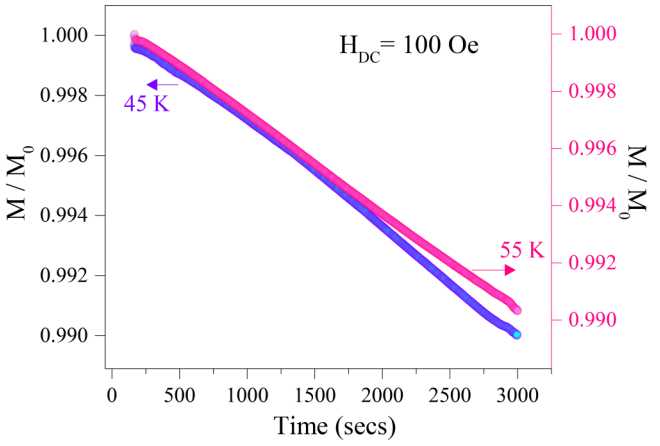

FIG. 14. The time dependence of normalized magnetization at chosen temperatures 45 K (left hand side) and 55 K (right hand side) of GSO9 under the field-cooled (FC) condition with $H_{DC} = 100$ Oe. The relaxation behavior of the GSO9 sample over time has been realized.

is calculated by the fraction of M_{FCW} to M_{FCC}. Figure 13(b) shows the invariant nature of δ over the broad temperature region of 40–160 K. The mean values of the phase fraction calculated are ∼70.65, 79.76, and 88.86% for $H_{DC} = 100$ Oe (pink), 400 Oe (blue), and 1000 Oe (green), respectively. Evidently, these values signify the comparative number of spins aligned to the AFM phase during the FCW protocol, where some of the AFM phase restricts itself while cooling under the same field, and the remaining fraction (1-δ) represents the FM clusters to the frozen AFM phase (by values of 29.35, 20.24, and 11.14%, respectively, for 100, 400, and 1000 Oe).

To further study the metastable glassy behavior associated with GSO9, the time-dependent magnetization is measured at 45 and 55 K (as shown in Fig. 14) and 6 K (not shown). For each measurement, the investigated system is cooled from room temperature (300 K) to 6 K under $H_{DC} = 100$ Oe and kept for 10 min for a homogenous spread of the temperature throughout the domains inside, after which the field was reduced to zero, the system was warmed to the measured temperatures (i.e., to 45 and 55 K), and the magnetization was recorded as a function of time for 60 min. The magnetization curve plotted in Fig. 14 is normalized with respect to the primary magnetization at $t = 0$. The strong relaxation in the magnetization behavior can be observed at both temperatures. The phase fraction AFM/FM clusters start to get arrested on cooling from 300 K in the presence of the field and stay intact with the removal of the field. The normalized magnetization starts to decrease with time because the local free energy of the remaining phase fraction gets utilized to convert the system to sustainable AFM phase. With the increase of temperature, the local free energy barrier increases sharply as the phase fraction is more at higher temperature, so the phase transition rate slows down a bit at higher temperatures [13].

C. Time dependence of magnetization

To determine the alteration in polarity of magnetization, magnetic switching experiments were conducted at suitable temperatures using both the FCC (70 K) and ZFCW (180 K)

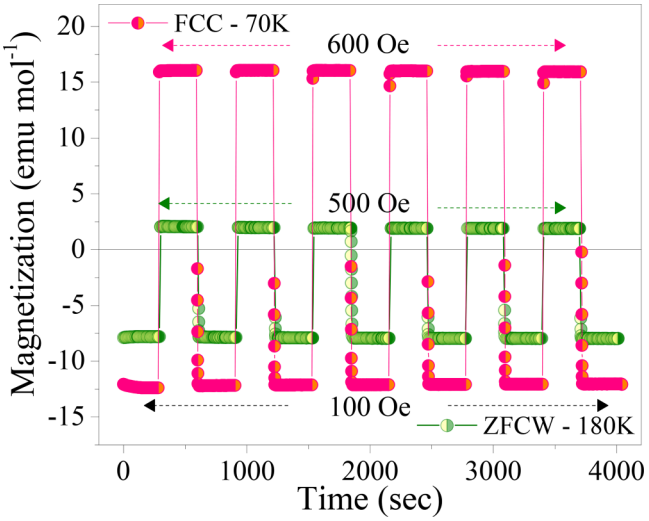

FIG. 15. The time dependence of magnetization $M(t)$ at 180 K [zero-field-cooled warming (ZFCW), green] and 70 K [field-cooled cooling (FCC), pink] measured at fields varying between 100 and 500 Oe and 100 and 600 Oe, respectively, for GSO5. The switching of the polarity of magnetization with respect to the field has been considered a parameter to stabilize M at each state for a period of 300 s.

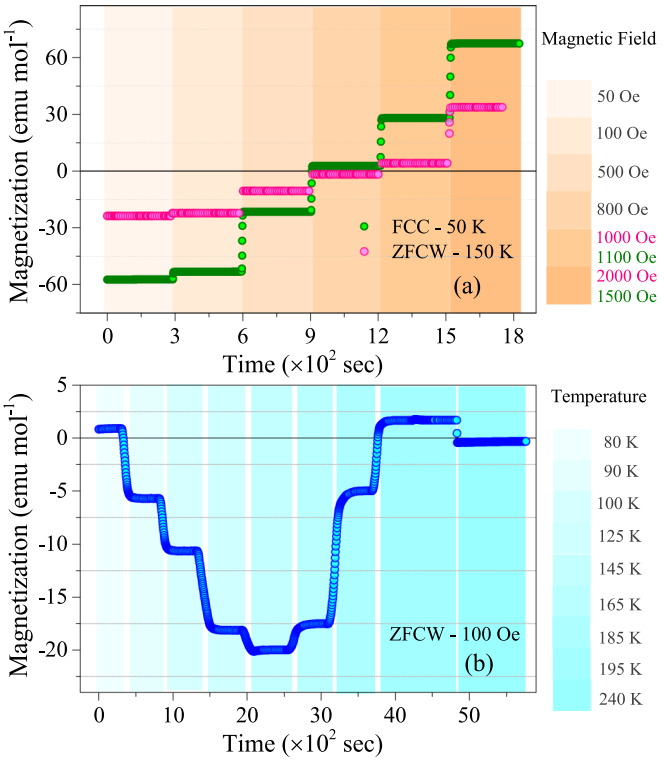

FIG. 16. (a) Time variation of magnetization $M(t)$ measured at different fields at constant temperatures $T = 50$ K [field-cooled cooling (FCC), orange] and $T = 150$ K [zero-field-cooled warming (ZFCW), blue]. (b) Magnetization variation with respect to time at different temperatures under ZFCW protocol (at 100 Oe field). For data recording at each stable condition, 300 s of the holding time is maintained during the measurement. The tuning of different stable states in both positive and negative magnetizations with respect to field and temperature has been quite obvious for GSO5 system.

protocols for GSO5, as depicted in Fig. 15. To understand the magnetization switching, the sample was cooled from paramagnetic temperature ($T > T_N$) to 180 K (near T_N), and an external field (H_{DC}) of 100 Oe was applied and kept constant for 5 min. After this, the field has been increased to 600 Oe, which was fixed for 5 min. This cycle is repeated several times to verify the reproducibility of the switching behavior. Such identical reversible bipolar switching of magnetization was performed for the FCC protocol as well at a temperature (70 K) below T_{Comp1}. Here, the sample was cooled until 70 K from room temperature under $H_{DC} = 100$ Oe, and the sequence was repeated several times (100 Oe → 600 Oe → 100 Oe) with a stability time of 5 min duration between each field change. The stability after the removal of the external field corresponding to each state has been detected without any significant decay of magnetization. For the 100 Oe field, combined magnetization remains in the negative state with spins aligning antiferromagnetically to each other when the higher field (500 and 600 Oe) flips the spins in the opposite direction, causing the net magnetization to be positive. It is interesting to note that the magnetization can be switched from positive to negative by changing H_{DC} to values in the same direction instead of switching the field direction as those in FM systems. The very existence of these two different polarity magnetization states varying with external actuator like magnetic field approves the application of this material in volatile magnetic memories, including in magnetic switches and magnetic data storage devices [52].

The stability of the negative magnetization has been ascertained for the same sample by time-dependent magnetization behavior for both ZFCW and FCC cases, keeping field and temperature as variable parameters, as shown in Figs. 16(a) and 16(b). Here, the sample was cooled from 300 to 150 K (50 K) under $H_{DC} = 0$ Oe ($H_{DC} = 100$ Oe) and was kept for a short duration of 2 min for homogeneity of the thermal alignment of the spins followed by field variations of 50, 100, 500, 800, 1000 (1100), and 2000 (1500) Oe, with 5 min of hold time at each field for data recording with respect to time, plotted in Fig. 16(a). For Fig. 16(b), the sample was cooled from the paramagnetic temperature region to 80 K with no external field applied, and data were recorded for 5 min of duration before the temperature was changed to 90 K, then further repetition of measurement to different temperatures (100, 125, 145, 165, 185, 195, and 240 K) for $H_{DC} = 100$ Oe. The accurate and stable negative magnitudes of magnetization can be noted for lower fields (∼50 Oe) and spontaneous polarity switching for higher field (1000 Oe). The change in the magnetic field and temperature has been shown by the different shades of color. The negative amplitudes for fixed field magnetization between T_{Comp1} and T_N with maximum negative moment of ~ -19 emu/mol follows the MT data showing the negative moment of ~ -17 emu/mol (see Fig. 8). The time-dependent magnetization data demonstrate consistent polarity switching behavior across different temperatures and magnetic fields. This finding suggests that the investigated system holds potential for utilization in large-scale switching devices due to its ability to perform multiple switching applications [8].

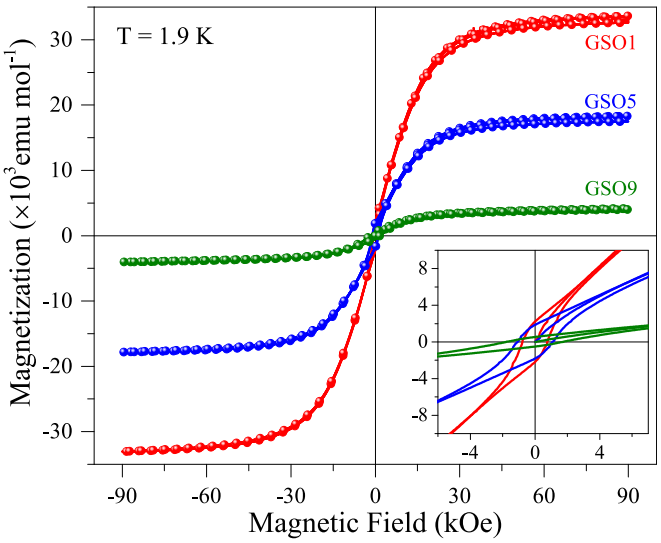

FIG. 17. The field dependence of magnetization (M-H) typical 5-cycle hysteresis loops at 1.9 K within ±90 kOe for GSO1 (red), GSO5 (blue), and GSO9 (green) under zero-field-cooled warming (ZFCW) protocol. The inset shows the enlarged view of the loops at the low magnetic fields (±60 kOe). The relative difference of saturation magnetization, coercivity, and exchange bias among the three compositions is quite interesting.

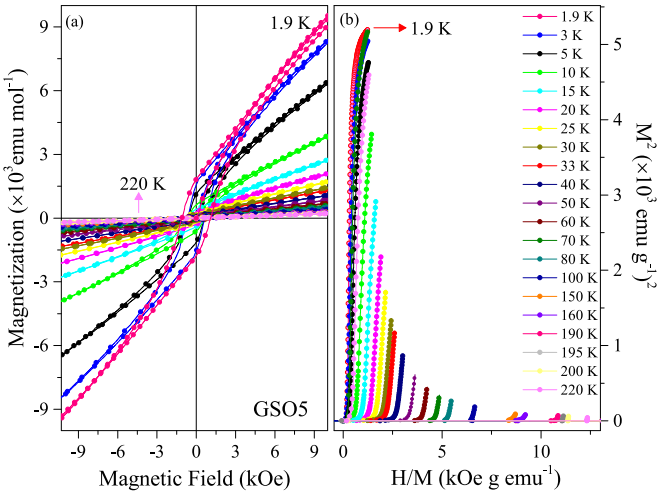

FIG. 18. (a) The field dependence of magnetization (M-H hysteresis loops) measured at different temperatures ranging from 1.9 to 220 K under zero-field-cooled warming (ZFCW) protocol for GSO5. (b) The Arrott plots (H/M vs M^2) calculated from the first quadrant isothermal magnetization curves of GSO5 within the temperature range 1.9–220 K. The gradual dominance of antiferromagnetic (AFM) character of the sample while moving toward T_N and the confirmation of second-order phase transition in GSO5 is quite evident.

D. Field dependence of magnetization

Figure 17 depicts the hysteresis loops of GSO1, GSO5, and GSO9 recorded within the field range of ±90 kOe at 1.9 K under standard ZFC mode. The inset shows an enlarged view of the respective plots at lower fields (±60 kOe), showing the finite coercivity and remanance. As predicted, the magnetization value drops to ∼87.7% (at +90 kOe) with increasing substitution of Sm (90%) at the Gd site. The insertion of Sm^{3+} at the A-site cationic position increases the AFM interaction and weakens the FM character in the system attained from Gd^{3+}, as evident from the decreasing moment and coercivity with increasing Sm substitution (as shown in the inset of Fig. 17). The hysteresis has been scarcely observed for GSO9, so the negligible amount of the remanance field indicates the prevalence of the weak FM Γ_4 phase at the low-temperature region. The remanance decreases from 2194 emu/mol to 548 emu/mol with the reduction of Sm substitution to 90 from 10%, where the coercivity increases from 14 kOe (GSO1) to 15.5 kOe (GSO9). The overall decrease of the magnetization is due to the lower moment of Sm^{3+} (∼0.84 μ_B) as compared with Gd^{3+} (∼7.94 μ_B). To explore the influence of different cations on magnetic anisotropy, the magnitude of the anisotropy constant (K_1), anisotropy field (H_K), and saturation magnetization (M_S) are calculated using the law of approach to saturation (LAS) [28]. The experimentally obtained first-quadrant M-H virgin curves are fitted with the LAS expression and extracted parameters given above are listed in Table 4s in the Supplemental Material [21] for all three compositions. From this analysis, it is very clear that K_1 falls rapidly to $\frac{1}{6}$th of the value of GSO1 to GSO9 due to the lower magnetocrystalline anisotropy and flexibility of rotation of the spins from the easy axis. However, the magnitude of anisotropy does not show any systematic variation, except it reaches ∼ 2207 kOe and 1375 kOe (GSO1).

For a better understanding of the domain dynamics of GSO5, a detailed field-dependent study at different temperatures has been performed. As described above, typical five-cycle M-H loops (±90 kOe) were measured under ZFC mode at various temperatures between 1.9 and 220 K (above T_N). Here, the M-H data have been collected with a field sweep of 200 Oe/min, and before the commencement of each measurement, the sample temperature has been upraised above T_N to attain a perfect randomization of the spin to bring the virgin state. In Fig. 18(a), the recorded data at certain temperatures are plotted to depict that the moments of the constituent elements cannot attain saturation even up to 90 kOe external field. For $T > 160$ K, the curves became almost straight lines, signifying the strong AFM component dominating over the FM component. On the other hand, Fig. 18(b) shows the Arrott plots (M^2 vs H/M) made from the M-H isotherms recorded at different temperatures, which show positive slopes near T_N, signifying the second-order phase transition from the disordered paramagnetic state to the AFM phase in GSO5, which is in line with the previous discussions. Nevertheless, all M-H loops exhibit asymmetry in their position (H_{C1} and H_{C2}) on either side of the loop, causing finite exchange bias field [$H_{EB} = (H_{C1} + H_{C2})/2$] even under the ZFC condition. The temperature dependences of both H_{EB} and $H_C[=(H_{C1} - H_{C2})/2]$ are shown in Figs. 19(a) and 19(b). The weak FM character induced by the anisotropic DM interaction in this AFM perovskite system is the main origin of the loop asymmetry in which the equivalent AFM and FM components play a significant role in deciding the

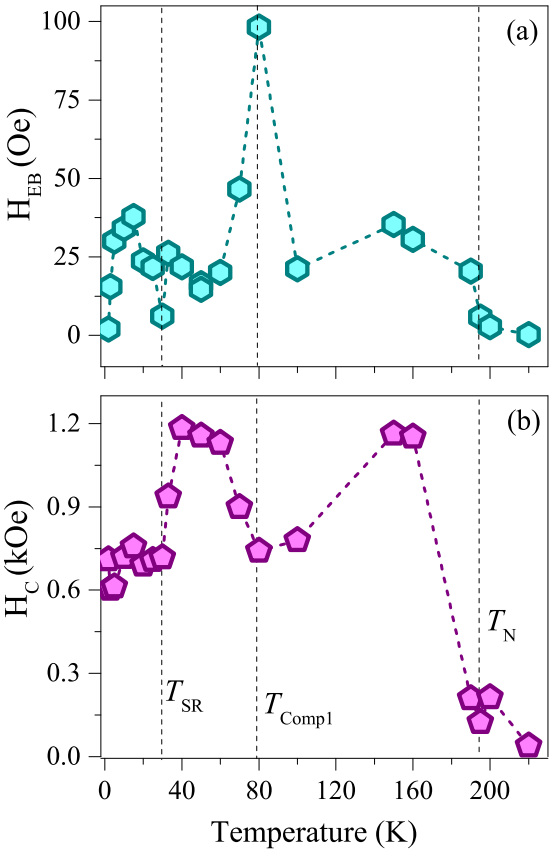

FIG. 19. The temperature variation of exchange bias $H_{EB}(T)$ and coercive field $H_C(T)$ of GSO5 measured under zero-field-cooled warming (ZFCW) protocol in the temperature range of 1.9–220 K. The anomalies in H_{EB} and H_C corresponding to transition temperatures for GSO5 are quite significant.

magnitude of H_{EB}. Clear anomalies were visible in the plots of $H_{EB}(T)$ and $H_C(T)$ at the characteristic temperatures T_{SR}, T_{Comp1}, and T_N. Both quantities increase slowly below T_N and show a divergence at T_{Comp1}, with a sudden fall to 6.2 and 717 kOe, respectively, near T_{SR}. A prominent change in the slope of $H_{EB}(T)$ and $H_C(T)$ across 195 K indicates the onset of the spin alignment in the AFM Γ_4 (G_x, A_y, F_z) phase. Moreover, a gradual increment in both $H_{EB}(T)$ and $H_C(T)$ was evident below T_N due to strong anisotropy of trivalent Cr ions, which holds the spins along the easy-axis direction of the G-type AFM component usually ordered along the x direction. These spins start rotating around the z axis and thus influence the FM component, which moves away from the easy axis as T approaches T_{Comp1} (here ∼80 K) down to T_{SR} (here ∼30 K), where the complete rotation is executed, as precluded in the previous section.

E. Magnetic phase diagram

After gathering the important results obtained above pertaining to both magnetic and structural data along with spectroscopic data of different compositions of the GSO systems, now we can shed light on the global magnetic phase diagram of this interesting perovskite system. Figures 20 and 21 represent the variation of magnetic ordering temperatures plotted as a function of field (T-H) obtained from the temperature and field-dependence magnetization data recorded under both ZFCW and FCC conditions, respectively, for all three investigated systems GSO1, GSO5, and GSO9. The solid orange spheres represent the magnitude of T_N, while the striped region shown below is designated as the Γ_4 (G_x, A_y, F_z) AFM phase. Here, the magnetic phases are not restricted in the narrow shaded portion; instead, they just indicate the different magnetic phases, as the region is broader, which are spreading until the next phase occurs. On the other hand, the data points

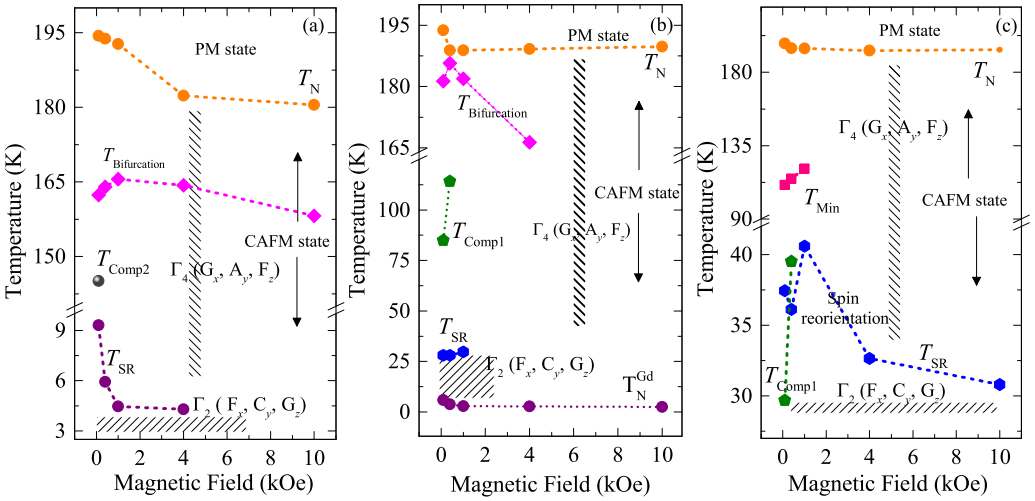

FIG. 20. The field-temperature (H-T) phase diagram of (a) GSO1, (b) GSO5, and (c) GSO9 mapped from the various parameters obtained from the magnetic measurements performed under the zero-field cooled (ZFC) protocols. The solid symbols represent the data points obtained from the experiments, while solid lines connecting the data points serve as visual guides. The shaded regions separate the boundary of a magnetic phase of the investigated systems, i.e., Γ_4 and Γ_2. Here, the compensation temperatures (T_{Comp1}, T_{Comp2}), bifurcation temperature ($T_{Bifurcation}$), maximum negative magnetization (T_{Min}), spin-flip temperature (T_{SF}), spin-reorientation temperature (T_{SR}), and ordering temperature of Gd (T_N^{Gd}) are represented with the respective symbols. In the present case, all data points shown in the H-T plane have been taken under zero-field-cooled warming (ZFCW) protocol.

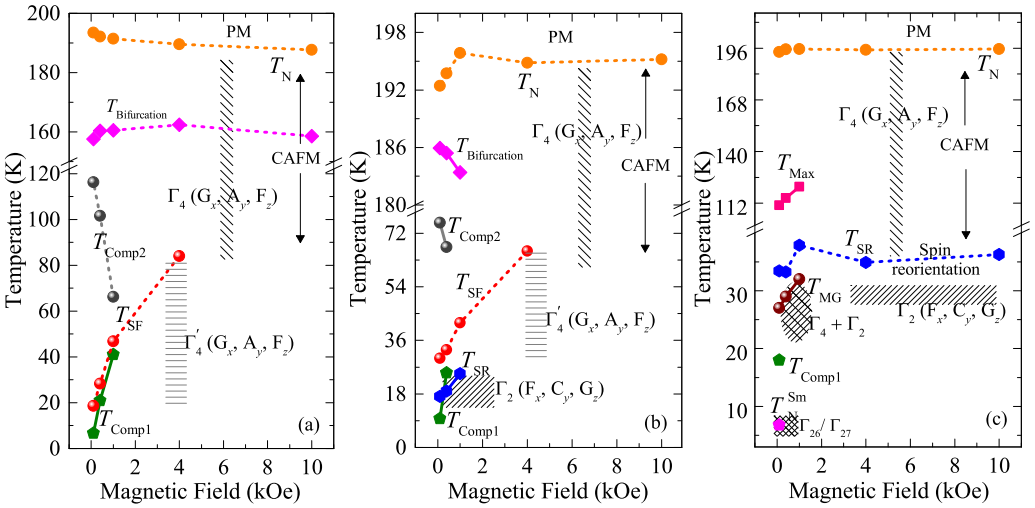

FIG. 21. The field-temperature (*H*-*T*) phase diagram of (a) GSO1, (b) GSO5, and (c) GSO9 mapped from the various parameters obtained from the magnetic measurements performed under the field-cooled cooling (FCC) protocol. The solid symbols represent the data points obtained from the experiments, while solid lines connecting the data points serve as visual guides. The shaded regions separate the boundary of a magnetic phases (Γ_4, Γ_2, Γ_{26}/Γ_{27}) of the investigated systems, i.e., Γ_4 and Γ_2. Here, the compensation temperatures (T_{Comp1}, T_{Comp2}), bifurcation temperature ($T_{Bifurcation}$), maximum negative magnetization (T_{Min}), spin-flip temperature (T_{SF}), spin-reorientation temperature (T_{SR}), and ordering temperature of Sm (T_N^{Sm}) are represented with the respective symbols. Here, the change in the spin direction is keeping the magnetic phase intact. In the present case, all data points shown in the *H*-*T* plane have been taken under field-cooled cooling (FCC) protocol.

represented by solid squares in magenta refer to $T_{Bifurcation}$, which diminishes at higher field (4000 Oe, ZFCW case) for the GSO5 sample; however, this variation completely vanishes for the GSO9 composition. The phase remains as canted AFM Γ_4, as no change in the magnetic ordering was noticed. The crossing of zero net magnetization across T_{Comp2} shown in dark gray spheres (prominently noticed in the FCC protocol) for 10 and 50% Sm substituted systems for a certain magnetic field upon decreasing the temperature is very prominent in the phase diagram, as the temperature is decreased with the rates 43 and 10.77%, respectively. For the ZFCW case, the magnetic compensation cannot take place, except for the GSO1 system at 100 Oe, as the combined induced field including the magnetocrystalline anisotropy field of Cr^{3+} and rare-earth cations are weaker than the applied external field. Another compensation T_{Comp1} arises at lower temperature for all samples (FCC) for a very specific span of temperature 7–40 K due to the activity of the rare-earth cations at lower temperature keeping the Γ_4 ($G_x, A_y,\ F_z$) magnetic structure intact [shown in green pentagon symbols of Fig. 21(c)]. Here, T_{SF} has been shown with red spheres, below which the Γ_4' state is designated as horizontal lines. Upon lowering the temperature to 37 K (for GSO9) in the ZFCW condition, the dominating AFM component orients along the crystallographic z axis, making the anisotropy energy low enough to allow the spins to make a transition to different magnetic phase Γ_2 with the dominant FM component toward the easy axis. Such reorientation T_{SR} is recognizable in all three compositions, shown by the blue color hexagon and the slanted lines, representing the associated Γ_2 phase. In the investigated systems, the contribution of Gd and Sm spins is very prominent at low temperatures, and we present their ordering temperatures T_N^{Gd} and T_N^{Sm} with purple and magenta symbols, respectively (Figs. 20 and 21). The spin-reorientation temperature overlaps with T_N^{Gd} for GSO1, making the phase transition <9.3 K for the ZFCW protocol, and gradually decays to 4.3 K with the increasing field value of 4000 Oe. For GSO9, the Sm ordering induces the change in the magnetic phase to either Γ_{26} (C_x , G_y , C_x ; C_x^R, A_y^R, F_z^R) or Γ_{27} (F_x , C_y , G_z ; F_x^R, C_y^R, G_z^R) only at low field of 100 Oe under the FCC case. The magnetic glass signature with a mixed phase of Γ_4 and Γ_2 configuration in the form of frozen FM and AFM clusters in the narrow temperature range of 27–32 K is labeled as maroon spheres (Fig. 21). The frozen spins exhibit a limited persistence beyond a certain threshold of applied field, thereby rendering the metastable phase more susceptible. Overall, we find that the implementation of various external probes to study the global magnetic behavior enriches the understanding of spin dynamics of GSO system

V. CONCLUSIONS

In conclusion, a strong correlation has been established between the crystal structure, phonon spectra, and magnetic properties of Sm-substituted $GdCrO_3$ perovskites by means of a comprehensive study of XRD, Raman, and DC magnetization, respectively. The investigated system undergoes a G-type AFM phase transition at $T_N = 197$ K (GSO1) to 201 K (GSO9) with Cr^{3+} along with Gd^{3+} and Sm^{3+} ions aligned in the Γ_4 ($G_x, A_y,\ F_z$) configuration. All three compositions show multiple crossovers or polarity changes in the magnetization measured under ZFCW, FCC, and/or FCW protocols. At lower temperatures <40 K, the anisotropic exchange interaction between rare earth and Cr^{3+} rotates the AFM component along the z axis from the easy axis, and the magnetic phase changes to the Γ_2 ($F_x, C_y,\ G_z$) configuration. The Sm-rich GSO9 shows the interesting characteristics of

the magnetic-field-driven short-range metastable frozen state of simultaneous existence of both Γ_2 (F_x, C_y, G_z) and Γ_4 (G_x, A_y, F_z) phases as the FM clusters in the AFM background matrix for the FCW case, which ceases to exist for higher magnetic field. Clear anomalies are detected in the Raman spectra across the magnetic ordering temperatures, specifying the direct spin-phonon coupling present in the system. In this paper, we also reveal gradual hardening of the $A_{1g}(5)$ mode $\sim 563\,\mathrm{cm}^{-1}$ with respect to temperature, which assures the Cr^{3+}-Cr^{3+} AFM coupling interaction complemented by the exchange-striction effect. The variation of the tilt angles, as calculated from refined structural parameters of XRD, engages in the quasiharmonic effect due to Gd^{3+}-Cr^{3+} exchange interaction, which softens the $A_{1g}(3)$ mode. Across the different substitution levels, the GSO shows multiple magnetic compensations under the ZFCW, FCC, and FCW cases. Overall, the intriguing characteristics explored under the substitution of Sm^{3+} in $GdCrO_3$ make it a potential candidate for applications in the field of tunable thermomagnetic switching devices, magnetic sensors, and nonvolatile magnetic memory storage devices.

ACKNOWLEDGMENTS

S.D. acknowledges the FIST program of the Department of Science and Technology (DST), India, for partial support of this paper (Files No. SR/FST/PSII-020/2009 and No. SR/FST/PSII-037/2016). S.T. acknowledges the DST Science and Engineering Research Board Core Research Grant File No. CRG/2022/006155 for the support of this paper. R.K.D. acknowledges the financial support from the Council of Scientific and Industrial Research, Ministry of Science and Technology, the Ministry of Education, Government of India. S.T. acknowledges the partial support from UGC-DAE CSR through a Collaborative Research Scheme Project No. CRS/2021–22/01/383. S.D. and R.K.D. would also like to acknowledge the Central Instrument Facility, IIT Guwahati, Project No. SR/FST/ETII-071/2016(G) dated 1.5.2017, and North East Centre for Biological Sciences and Healthcare Engineering, IIT Guwahati, and Department of Biotechnology, Government of India, with Project No. BT/COE/34/SP28408/2018 for the partial support of this paper.

[1] E. F. Bertaut, G. Bassi, G. Buisson, P. Burlet, J. Chappert, A. Delapalme, J. Mareschal, G. Roult, R. Aleonard, R. Pauthenet *et al.*, J. Appl. Phys. **37**, 1038 (1966).
[2] C. R. Serrao, A. K. Kundu, S. B. Krupanidhi, U. V. Waghmare, and C. N. R. Rao, Phys. Rev. B **72**, 220101(R) (2005).
[3] B. Rajeswaran, D. I. Khomskii, A. K. Zvezdin, C. N. R. Rao, and A. Sundaresan, Phys. Rev. B **86**, 214409 (2012).
[4] K. R. S. Preethi Meher, A. Wahl, A. Maignan, C. Martin, and O. I. Lebedev, Phys. Rev. B **89**, 144401 (2014).
[5] N. Shamir, H. Shaked, and S. Shtrikman, Phys. Rev. B **24**, 6642 (1981).
[6] L. Neel, Ann. Phys. **12**, 137 (1948).
[7] A. Kumar and S. M. Yusuf, Phys. Rep. **556**, 1 (2015).
[8] A. Pal, M. Mohan, A. Venimadhav, and P. Murugavel, Phys. Rev. Mater. **4**, 044407 (2020).
[9] M. Tripathi, T. Chatterji, H. E. Fischer, R. Raghunathan, S. Majumder, R. J. Choudhary, and D. M. Phase, Phys. Rev. B **99**, 014422 (2019).
[10] K. Yoshii, J. Solid State Chem. **159**, 204 (2001).
[11] T. Sau, P. Yadav, S. Sharma, R. Raghunathan, P. Manuel, V. Petricek, U. P. Deshpande, and N. P. Lalla, Phys. Rev. B **103**, 144418 (2021).
[12] M. Ohkoshi, H. Kobayashi, T. Katayama, and M. Hirano, IEEE Trans. Magn. **13**, 1158 (1977).
[13] T. Sarkar, V. Pralong, and B. Raveau, Phys. Rev. B **83**, 214428 (2011).
[14] P. Chaddah, K. Kumar, and A. Banerjee, Phys. Rev. B **77**, 100402(R) (2008).
[15] M. Manekar, M. K. Chattopadhyay, and S. B. Roy, J. Phys.: Condens. Matter **23**, 086001 (2011).
[16] M. K. Chattopadhyay, S. B. Roy, and P. Chaddah, Phys. Rev. B **72**, 180401(R) (2005).
[17] S. B. Roy, M. K. Chattopadhyay, P. Chaddah, J. D. Moore, G. K. Perkins, L. F. Cohen, K. A. Gschneidner Jr., and V. K. Pecharsky, Phys. Rev. B **74**, 012403 (2006).
[18] X. L. Qian, J. Kang, B. Lu, S. X. Cao, and J. C. Zhang, RSC Adv. **6**, 10677 (2016).
[19] S. Mahana, U. Manju, and D. Topwall, J. Phys. D: Appl. Phys. **51**, 305002 (2018).
[20] G. Gorodetsky, R. M. Hornreich, S. Shaft, B. Sharon, A. Shaulovand, and B. M. Wanklyn, Phys. Rev. B **16**, 515 (1977).
[21] See Supplemental Material at http://link.aps.org/supplemental/10.1103/PhysRevMaterials.7.084410 for supplemental data consists of crystallographic parameters of different compositions of $Gd_{1-x}Sm_xCrO_3$ obtained from the Rietveld refinement of the XRD data, list of Raman modes, relevant Lorentzian fitting parameters of A_{1g} (6) mode and various parameters obtained from the temperature and field dependence of magnetization data.
[22] P. Gupta, R. Bhargava, and P. Poddar, J. Phys. D: Appl. Phys. **48**, 025004 (2015).
[23] R. D. Shannon, Acta Cryst. A **32**, 751 (1976).
[24] A. Durán, R. Escamilla, R. Escudero, F. Morales, and E. Verdín, Phys. Rev. Mater. **2**, 014409 (2018).
[25] A. Nashim and K. M. Parida, Chem. Eng. J. **215**, 608 (2013).
[26] V. K. Shen, D. W. Siderius, W. P. Krekelberg, and H. W. Hatch, NIST Standard Reference Simulation Website, NIST Standard Reference Database Number 173, National Institute of Standards and Technology, Gaithersburg MD, 20899.
[27] R. K. Dokala, S. Das, B. Weise, R. Medwal, R. S. Rawat, and S. Thota, J. Phys.: Condens. Matter **34**, 065801 (2022).
[28] S. Das, R. K. Dokala, B. Weise, R. Medwal, R. S. Rawat, P. K. Mishra, and S. Thota, J. Phys.: Condens. Matter **34**, 345803 (2022).
[29] A. Jaiswal, R. Das, S. Adyanthaya, and P. Poddar, J. Nanopart. Res. **13**, 1019 (2011).
[30] H. Zhang, H. Peng, L. Xie, Z. Wang, L. Liu, X. He, and Y. Li, J. Supercond. Nov. Magn. **34**, 1415 (2021).
[31] A. M. Glazer, Acta Cryst. B **28**, 3384 (1972).

[32] A. A. A. Qahtan, S. Husain, A. Somvanshi, W. Khan, and Y. K. Manea, J. Mater. Sci.: Mater. Electron. **31**, 9335 (2020).
[33] P. Gupta and P. Poddar, RSC Adv. **5**, 10094 (2015).
[34] M. El Amrani, M. Zaghrioui, V. Ta Phuoc, F. Gervais, and N. E. Massa, J. Magn. Magn. Mater. **361**, 1 (2014).
[35] S. Mahana, B. Rakshit, R. Basu, S. Dhara, B. Joseph, U. Manju, S. D. Mahanti, and D. Topwal, Phys. Rev. B **96**, 104106 (2017).
[36] A. Sarkar, B. Dalal, and S. K. De, J. Phys.: Condens. Matter **31**, 505801 (2019).
[37] M. C. Weber, J. Kreisel, P. A. Thomas, M. Newton, K. Sardar, and R. I. Walton, Phys. Rev. B **85**, 054303 (2012).
[38] J. Andreasson, J. Holmlund, C. S. Knee, M. Käll, L. Börjesson, S. Naler, J. Bäckström, M. Rübhausen, A. K. Azad, and S. G. Eriksson, Phys. Rev. B **75**, 104302 (2007).
[39] E. Granado, A. García, J. A. Sanjurjo, C. Rettori, I. Torriani, F. Prado, R. D. Sánchez, A. Caneiro, and S. B. Oseroff, Phys. Rev. B **60**, 11879 (1999).
[40] M. Balkanski, R. F. Wallis, and E. Haro, Phys. Rev. B **28**, 1928 (1983).
[41] Y. Sharma, S. Sahoo, W. Perez, S. Mukherjee, R. Gupta, A. Garg, R. Chatterjee, and R. S. Katiyar, J. Appl. Phys. **115**, 183907 (2014).
[42] J. Guo, Y. Su, C. Shi, G. Gong, X. Cheng, X. Zhu, H. Hu, and Y. Wang, J. Supercond. Nov. Magn. **35**, 711 (2022).
[43] I. Dzyaloshinsky, J. Phys. Chem. Solids **4**, 241 (1958).
[44] E. F. Bertaut, Acta Cryst. A. **24**, 217 (1968).
[45] A. Banerjee, K. Mukherjee, Kranti Kumar, and P. Chaddah, Phys. Rev. B **74**, 224445 (2006).
[46] L. B. Mendelsohn, F. Biggs, and J. B. Mann, Phys. Rev. A **2**, 1130 (1970).
[47] T. Moriya, Phys. Rev. **120**, 91 (1960).
[48] A. Cooke, D. Martin, and M. Wells, J. Phys. C: Solid State Phys. **7**, 3133 (1974).
[49] K. Yoshii, Mater. Res. Bull. **47**, 3243 (2012).
[50] X. L. Qian, D. M. Deng, Y. Jin, B. Lu, S. X. Cao, and J. C. Zhang, J. Appl. Phys. **115**, 193902 (2014).
[51] M. Tripathi, R. J. Choudhary, and D. M. Phase, RSC Adv. **6**, 90255 (2016).
[52] S. M. Yusuf, A. Kumar, and J. V. Yakhmi, Appl. Phys. Lett. **95**, 182506 (2009).